# Simulation of a Volumetric Receiver-Reactor

Dipl.-Ing. Reiner Buck

Forschungsbereich Energietechnik
Institut für technische Thermodynamik
Abteilung Solarenergiewandlung
Pfaffenwaldring 38/40
7000 Stuttgart 80

*Document Number Internal Report DLR - IB 91 102*

(2nd, revised edition)

*Stuttgart, January 14th, 1993*

*Solarenergie-Nutzung, thermodynamische Modellierung, volumetrische Receiver, poröse Absorber, chemischer Receiver-Reaktor, $CO_2$-Reformierung von Methan, Austauschfaktoren, Parameter-Studie*

**Simulation eines Volumetrischen Receiver-Reaktors**

**Übersicht**

Ein Modell zur Simulation volumetrischer Receiver-Reaktoren zur solaren Methanreformierung mit $CO_2$ wurde entwickelt und zur Nachrechnung von Experimenten des CAESAR-Projektes verwendet. Dabei zeigte sich eine gute Übereinstimmung zwischen gemessenen und berechneten Werten für den gesamten Receiver. Lokale axiale Temperaturverteilungen im Absorber wurden ebenfalls verglichen und ergaben unter Annahme eines örtlich reduzierten Massenstroms ebenfalls akzeptable Übereinstimmung. Darüberhinaus wurde mit einem einfachen Receivermodell eine Parameteranalyse für einen chemischen Receiver-Reaktor durchgeführt, um kritische Einflußgrößen zu ermitteln. Als kritische Parameter erwiesen sich dabei die katalytische Aktivität und die Anpassung zwischen solaren Strahlungsverhältnissen und Massenstrom, sowohl lokal als auch auf den gesamten Receiver bezogen. Im Hinblick auf gutes Systemverhalten erscheint vor allem die Einbeziehung eines Gegenstrom-Wärmetauschers empfehlenswert.

*Solar energy, thermodynamic modelling, volumetric receiver, porous absorber, chemical receiver-reactor, $CO_2$-reforming of methane, exchange factors, parameter study*

**Simulation of a Volumetric Receiver-Reactor**

**Summary**

A model was developed to simulate volumetric receiver-reactors for solar methane reforming with $CO_2$. This model was used to simulate experimental runs performed during the CAESAR project. The agreement between experiments and simulated performance was quite good for the overall receiver performance. Local axial temperature distributions were also compared and showed acceptable agreement when a locally reduced mass flow was assumed. With a simplified receiver model a parametric study was performed to identify critical design parameters. The results indicate great influence of the catalytic activity and of proper matching between solar flux density and mass flow, both locally and for the complete receiver. Concerning a good system performance the addition of a counterflow heat exchanger is of great importance.

## Contents

## List of Illustrations

## List of Tables

## Nomenclature

| | |
|---|---|
| $A$ | area ($m^2$) |
| $b$ | backscatter fraction (-) |
| $c_p$ | specific heat capacity ($J \cdot kg^{-1} \cdot K^{-1}$) |
| $E$ | thermal emission ($W \cdot m^{-2}$) |
| $f$ | forward scatter fraction (-) |
| $G$ | irradiance ($W \cdot m^{-2}$) |
| $h$ | convective heat transfer coefficient ($W \cdot m^{-2} \cdot K^{-1}$) |
| $\Delta H$ | heat of reaction ($kJ/mol$) |
| $I,J$ | radiant flux density ($W \cdot m^{-2}$) |
| $k_a$ | absorption coefficient ($m^{-1}$) |
| $k_s$ | scattering coefficient ($m^{-1}$) |
| $k_t$ | (total) extinction coefficient ($m^{-1}$) |
| $\dot{n}$ | molar flow ($mol/s$) |
| $m$ | mass (kg) |
| $P$ | power (W) |
| $PPI$ | Pores per (linear) inch |
| $p$ | pressure (bar) |
| $q$ | heat flux ($W \cdot m^{-2}$) |
| $r$ | specific reaction rate ($mol \cdot s^{-1} \cdot kg_{cat}^{-1}$) |
| $Y$ | exchange factor (-) |

**Greek Symbols:**

| | |
|---|---|
| $\alpha$ | absorptivity (-) |
| $\Gamma$ | catalyst loading (% weight) |
| $\varepsilon$ | emissivity (-) |
| $\eta$ | efficiency (-) |
| $\lambda$ | wavelength ($m$), thermal conductivity ($W \cdot m^{-1} \cdot K^{-1}$) |
| $\mu$ | cosine of incidence angle (-) |
| $\omega$ | albedo (-) |
| $\chi$ | methane conversion (-) |
| $\psi$ | porosity (-) |
| $\rho$ | reflectivity (-); density ($kg/m^3$) |
| $\tau$ | transmissivity (-); optical depth (-) |

**Indices:**

| | |
|---|---|
| *a,abs* | absorption, absorber |
| *cat* | catalyst, catalytic |
| *ch* | chemical |
| *dif* | diffuse |
| *inc* | incident, incidence |
| *IR* | infrared |
| *reac* | reaction |
| *rec* | receiver |
| *S* | Solar |
| *sp* | specular |

## 1. Introduction

The application of concentrated solar energy for chemical reactions has come into the focus. The transformation of radiation into energy-delivering chemical reactants might help to solve the problem of storing and transportation of solar energy. Another application is the direct use of solar high-energy photons to drive specific reactions (i. e. photoenhancement, photo-catalysis). Research work on the following applications is performed in various institutions:

- chemical heat pipe systems for transportation and storage of solar energy using a closed loop
- production of solar fuels and chemicals
- solar water treatment and detoxification of hazardous wastes
- use of solar high-energy photons to perform specific reactions

In 1987 a joint project between Sandia National Laboratories, Albuquerque (SNL), NM, and DLR Stuttgart, FRG, was started to demonstrate solar reforming of methane with carbon dioxide. This 'proof of concept'-test was operated from 1989 until 1991 with encouraging results. Tests were run at power levels up to 100kW and at maximum methane conversion levels of 70%. Receiver and chemical efficiencies reached 85% and 54%, respectively (see [5]). The receiver used a direct-irradiated volumetric absorber to perform the chemical reaction. Absorber performance was quite satisfactory in promoting the chemical reaction, however problems like absorber cracking and catalyst deactivation occured.

The development of simulation models for volumetric receiver-reactors was part of the CAESAR project. Both SNL and DLR developed a code to theoretically investigate the performance of such systems. The SNL model concentrates on a flat absorber with a flat window, the DLR model is directed to treat the receiver as a complete system including three-dimensional interactions. Therefore complex (e.g. domed) absorber and window geometries could be simulated. Both models approximate the absorber as one-dimensional.

The goal of this development is twofold. First these models can be used to determine critical design parameters which influence the layout of the receiver. This was helpful during the design phase of the CAESAR receiver-reactor. As an example the choice of the absorber pore size could be mentioned.

The second goal is to provide the tools for future improvements for these systems and for the adaption of a receiver to a given concentrator unit. It is obvious that a receiver-reactor for a dish system looks quite different to a receiver for a tower plant where a modular design with secondary concentrators is required.

The development of simulation models should be done in combination with tests. The models were therefore used to calculate local temperature distributions and overall performance of the CAESAR receiver. Comparisons with the measured data of the CAESAR tests were then used to evaluate the models.

## 2. Description of the Simulation Model

The simulation model development at DLR Stuttgart, as part of the CAESAR project, was developed to perform theoretical investigations of complete receiver-reactors. Emphasis was on developing the capability to calculate the thermodynamic and chemical behaviour of receivers with complicated geometries which are expected as a result of optimization studies. Such a receiver will be composed of the following elements: absorber, window, fluid inlet (which might be built as an absorber too) and other zones (i.e. insulated receiver elements). Each of these elements might have a quite complex geometry (see Figure 33 on page 48). One major issue is therefore the total radiative exchange in the receiver which is treated in a 3-dimensional way. The absorber is then a sub-element of the complete receiver.

The developed simulation model combines the calculation of total radiation exchange in the receiver with the energy calculation for the absorber zones and other zones for which a certain heat flux could be defined (i.e. to account for conduction). A detailed description of the model can be found in [2]. The following sections give a short outline of the model.

### 2.1 Radiation Exchange in the Receiver

As a first step, the distribution of the concentrated solar flux on all receiver elements is calculated. This could be done by various methods. For simple geometries it is sufficient to know the local flux density on the aperture area (as calculated by the HELIOS code or measured with a flux mapper). For complex receiver geometries, ray tracing procedures are applied to calculate the distribution of incident collimated radiation on all participating elements. This requires knowledge of the angular flux distribution in the aperture of the receiver.

The calculated solar flux distribution is the starting point for the calculation of the net radiation exchange in the receiver which is based on the so-called 'zonal method'. A basic outline of the method is given in [3]. For the application to volumetric receivers with a quartz window covering the aperture it is essential to account for transmission and specular reflection. Therefore the zonal method was improved as described below.

The receiver is divided into N surface zones (or elements) each of them having homogeneous material properties and thermodynamical data over the zone surface. These zones are divided into three different types, as follows:

- type 1: the zone temperature is prescribed
- type 2: the heat flux of the zone is prescribed
- type 3: the diffuse radiation leaving the zone is prescribed

The radiative properties of the zones include specular and diffuse reflection, transmission and absorption. For each surface

$$\alpha + \tau + \rho_{dif} + \rho_{sp} = 1 \tag{1}$$

The radiation exchange could be formulated using a variable number of wavelength bands to account for spectral dependance of the properties (multi-band model).

For the calculation of radiation exchange the so-called **exchange factors** must be known. This exchange factor $Y^k_{i,j}$ defines the part of the diffuse radiation emitted from element **i** in the wavelength band **k** which arrives on element **j** both directly and by all possible intermediate reflections and transmissions. In case that no transmission and specular reflection occurs the exchange factor is equal to the configuration factor.

The determination of the exchange factor matrix could be derived from configuration factor tables (for simple geometries) or calculated by suitable methods (e.g. ray-tracing procedures with Monte-Carlo techniques).

For the zones of type 1 or 2 the diffuse radiation leaving zone $i$ is given by the sum of diffusely reflected irradiation and diffuse emission:

$$J_i^k = \rho_{dif,i}^k (G_i^k + G_{s,i}^k) + E_i^k \tag{2}$$

The thermal emission in wavelength band $k$ is defined by

$$E_i^k = \varepsilon_i^k f_{bb}^k \sigma T_i^4 \tag{3}$$

with $f_{bb}^k$ being the fraction of the black body radiation emitted in wavelength band $k$. Using the above definition of the exchange factors the diffuse irradiation of zone $i$ as

$$G_i^k = \sum_{j=1}^{N} Y_{i,j}^k J_j^k \tag{4}$$

For the zones with prescribed heat flux (type 2) the temperature must be determined first. The heat flux into the zone is the difference between absorbed and emitted radiation:

$$q_{ib} = \sum_{k=1}^{K} \{\alpha_{ib}^k (G_{ib}^k + G_{s,ib}^k) - E_{ib}^k\} \tag{5}$$

The index $ib$ refers here to the $ib$'th zone of type 2. The prescription for the heat flux could include several terms as follows

$$q_{ib} = q_{0,ib} + \frac{\lambda_{mat}}{s} (T_{ib} - T_{ref}) \tag{6}$$

This allows to account for fixed heat fluxes and for fluxes which depend on the temperature of the calculated element. The latter term specifies the heat flux by thermal conduction (1-dimensional) through a material with thickness $s$. The temperature $T_{ref}$ could be either fixed or variable. This is important to calculate the heat flux by conduction between the two surfaces of a window.

For the calculation of the total radiation exchange the absorber is simulated as a zone of type 3, that means with prescribed outgoing radiation $J^k$. The details of the absorber simulation are described in the next section. The described equations lead to a set of linear equations when no type 2 zones are included. If such zones are present a subset of nonlinear equations must be solved to determine the required zone temperatures.

### 2.2 Simulation of the Volumetric Absorber

The calculation of the steady state thermal and chemical conditions within the volumetric absorber takes the following energy transfer mechanisms into account:

- radiation (absorption, scattering, emission)
- convection between absorber and fluid
- sensible fluid heating
- change in fluid composition by chemical reaction

Heat conduction in the solid and the fluid is neglected since the mechanism of radiation transport is dominant at the temperatures existing in the absorber. The model allows one-

dimensional calculation of all properties. The absorber could be composed of multiple layers with different characteristics, but the layer itself is treated as a continuum. The radiation transport is be described by absorption and scattering coefficients with the same wavelength bands as in the receiver calculation. For the radiation a distinction is made between collimated and diffuse radiation. A modified Two-Flux-model is used to calculate the radiation distribution inside the absorber. The governing equations are described below. The index k (definining the wavelength band) is omitted here for convenience.

The collimated radiation impinging onto the absorber is separated into a number of N ranges with specific incidence angles $\mu$ relative to the absorber axis. The attenuation of this radiation is then given by

$$I_{c,n} = I_{c0,n} \cdot e^{-\frac{k_a + k_s}{\mu_n} z} \tag{7}$$

The two-flux equations could be derived as

$$\frac{dI^+}{dz} = -2(k_a + (1-f)k_s)I^+ + 2bk_sI^- + 2k_aI_B + \sum_{n=1}^{N} \frac{k_s}{\mu_n} fI_{c,n} \tag{8}$$

for the forward direction and

$$-\frac{dI^-}{dz} = -2(k_a + (1-f)k_s)I^- + 2bk_sI^+ + 2k_aI_B + \sum_{n=1}^{N} \frac{k_s}{\mu_n} bI_{c,n} \tag{9}$$

for the backward directed radiation. The emissive power is given by

$$I_B = f_{bb}\sigma T_a^4 \tag{10}$$

The boundary condition on the irradiated side of the absorber ($z = 0$) is

$$I^+ = I_0^+ \tag{11}$$

which is the sum of all diffuse irradiation parts. The boundary condition at the opposite side ($z = L$) is given by

$$I^- = \rho(I_L^+ + \sum_{n=1}^{N} I_{c,n}) + I_{BL} \tag{12}$$

assuming that the surroundings behind the absorber has an effective reflection of $\rho$.

The energy balance is based on two chemical reactions and sensible heating of the fluid. The main reaction is methane reforming with carbon dioxide (index j = 1) (the heat of reaction, $\Delta H$, is based on 0°C and 1 bar)

$$CH_4 + CO_2 \Rightarrow 2CO + 2H_2 \qquad (\Delta H = 246.4 kJ/mol) \tag{13}$$

This reaction is accompanied by the watergas shift reaction (index j = 2)

$$CO_2 + H_2 \Rightarrow CO + H_2O \qquad (\Delta H = 41.24 kJ/mol) \tag{14}$$

Other possible reactions are neglected.

The energy balance over the fluid leads to the differential equation

$$\frac{dT_f}{dz} = \frac{hA_{cV}}{(\dot{m}/A)\tilde{c}_p}(T_a - T_f) \tag{15}$$

The specific heat capacity is dependent on chemical composition and temperature of the fluid. The boundary condition for the fluid temperature is

$$T_{f,z=0} = T_{fluid,in} \tag{16}$$

For the absorber temperature no boundary condition is required. The energy balance for the solid is given by

$$\sum_{k=1}^{K}\{2k_a(I^+ + I^-) - 4k_a f_{bb}\sigma T_a^4 + \sum_{n=1}^{N}\frac{k_a}{\mu_n} I_{c,n}\} - hA_{cV}(T_a - T_f) - \sum_{j=1}^{2}\rho_{abs}\cdot r_j \cdot \Delta H_j = 0 \tag{17}$$

The reaction rates $r_j$ for both reactions are taken from [4]. These rates are derived for an alumina substrate with a washcoat on which rhodium is deposited as catalyst. The absorber density $\rho_{abs}$ is the density of the absorber structure including washcoat and catalyst. The heat of reaction is also dependent on fluid temperature.

The change in chemical composition for all participating species ($i = 1,5$) could be expressed as

$$\frac{d\dot{n}_i}{dz} = A\rho_{abs}\sum_{j=1}^{2}\nu_{i,j}r_j \tag{18}$$

where $\nu_{i,j}$ is the stochiometric factor of the species i in the reaction j. The boundary condition for the fluid composition is

$$\dot{n}_{i,z=0} = \dot{n}_{inlet} \tag{19}$$

## Calculation Procedure

The equations for the radiation distribution are solved separately using a finite difference sheme, whereas the equations for the fluid and absorber temperatures and chemical composition are solved with a Runge-Kutta procedure of fourth order.

The overall radiation exchange and the operation condition of the absorber and other elements are strongly dependent on each other. Therefore, various iteration levels are necessary to solve the complete system of equations. A FORTRAN-code called **TOTCRR** was developed at DLR Stuttgart to perform this task. The main steps of the calculation procedure are listed below. The solar flux distribution (calculated by a different code) is available as input data, as well as the exchange factor matrices for the given receiver geometry.

1. read in all input data: definition of zones, collimated solar flux distribution, receiver operation conditions (i.e. mass flow, pressure, feed gas composition), exchange factors, radiative properties, etc.
2. estimate initial values for radiation and absorber temperatures
3. calculate for all absorber elements:
   a. distribution of radiation throughout the absorber
   b. fluid and catalyst temperature profiles in the absorber, change of chemical composition of the fluid

c. check the results for convergence of fluid and absorber temperatures. If the convergence criterion is not reached, continue with step 3a).

As a result, the reradiation $J$ from all absorber zones (type 3) is available for the enclosure calculations.

4. calculate the temperature of zones having prescribed heat flux (type 2)

5. calculate the total radiation exchange between all elements of the receiver (absorber elements, window elements, insulated sections etc.). As a result, the (new) irradiation of all elements is obtained.

6. check the results for convergence of the irradiation of each zone. If the convergence criterion is reached, continue; else go back to step 3.

7. perform control calculations to ensure consistency of the results; store the results on file.

As an option, a desired methane conversion in the exit fluid could be specified. In this case, the mass flow is varied iteratively until the desired conversion is reached.

## 3. Simulation of the CAESAR Receiver-Reactor

To validate the theoretical modeling some representative tests with the CAESAR receiver-reactor were compared with simulation runs. The accuracy of each simulation model depends strongly on the input data. Therefore, the input data used in these comparisons is discussed in detail below.

### 3.1 Simulation Input data

The input data for a receiver calculation can be subdivided into two categories:

1. receiver data (fixed)
2. operation data (variable)

These two types of data are described more in detail in the following sections.

#### 3.1.1 Receiver Data

These data are fixed for a specific test setup (i.e. the receiver with the 1st absorber insert). Some data are common to all simulation runs, while others apply only to a limited number of runs. A schematic view of the receiver is given Figure 1.

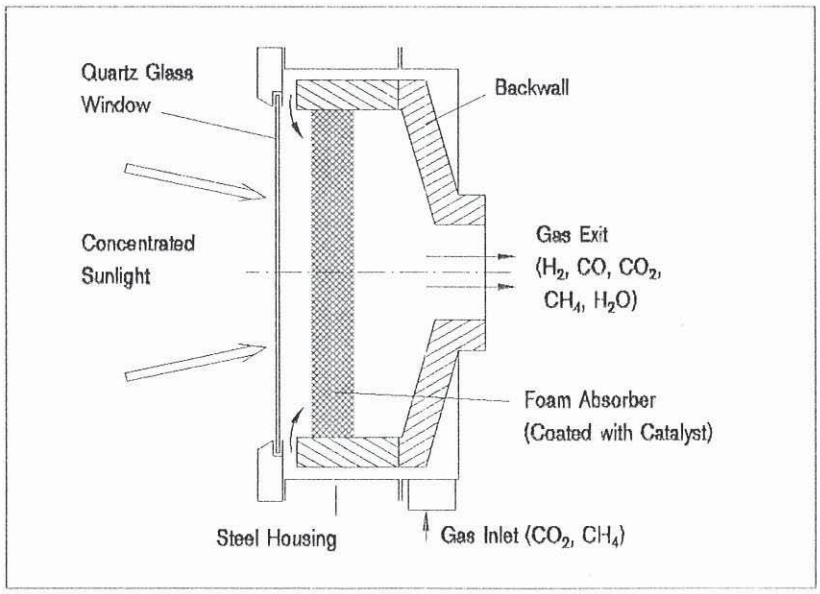


**Figure 1. Schematic of the CAESAR Receiver-Reactor**

The aperture diameter of the receiver is 60cm. This aperture is covered by a 10mm thick quartz window. The fluid is fed into the receiver on the back side, passes then through a ring channel and enters the 3cm gap between window and absorber over the whole circumferential length. While passing through the volumetric absorber, the fluid is heated and converted to synthesis gas. The reacted gas is collected and exhausted through a flare. A small portion of the exiting gas is quenched and fed into a gas analysis assembly for evaluation of composition.

For the simulation the receiver is divided into 29 model zones (or elements). A complete description of these zones is given in Table 16 on page 51. Zones 1 through 9 are sections

of the absorber, zone 10 is the annular fluid inlet section, zones 11 through 28 are inner and outer surface elements of the quartz window and the aperture is zone 29. Here the aperture is modeled as an imaginary plane which absorbs all irradiation (to simulate that all radiation passing the aperture from inside the receiver is completely lost). The location of the aperture is identical with zones 20 through 28. The definition of this imaginary zone is necessary to define a complete enclosure for the zonal method calculation.

The zone division is for simplicity reasons chosen according to the absorber part division. Each absorber zone in the model corresponds to an absorber piece of the CAESAR absorber, and the division of the outer and inner surface of the quartz window into zones is equal to the absorber partitioning.

The exchange factors for this configuration were determined using a Monte-Carlo ray-tracing technique, as described in [2]. The wavelength range was divided into two bands, the solar band (index S) with $0 \leq \lambda \leq 3\mu m$ and the infrared band (index IR) with $\lambda > 3\mu m$. The radiative properties used for the calculation are listed in Table 1. This table does not contain the diffuse reflectance which could be obtained from (1) on page 2. For the calculation, the absorber was assumed to be black, which does not lead to an error since diffuse reflection is treated within the zonal method (unless no specular reflection and transmission occurs at the absorber).

| | $\alpha_S$ | $\alpha_{IR}$ | $\tau_S$ | $\tau_{IR}$ | $\rho_{S,sp}$ | $\rho_{IR,sp}$ |
|---|---|---|---|---|---|---|
| absorber | 1.0 | 1.0 | 0.0 | 0.0 | 0.0 | 0.0 |
| ring wall | 0.5 | 0.5 | 0.0 | 0.0 | 0.0 | 0.0 |
| window (quartz) | 0.02 | 0.95 | 0.90 | 0.0 | 0.08 | 0.05 |
| aperture | 1.0 | 1.0 | 0.0 | 0.0 | 0.0 | 0.0 |

**Table 1. Exchange Factor Calculation: Radiative Properties of the Receiver Elements**

From the calculation for each wavelength band a matrix with 29x29 elements is obtained containing all the required exchange factors.

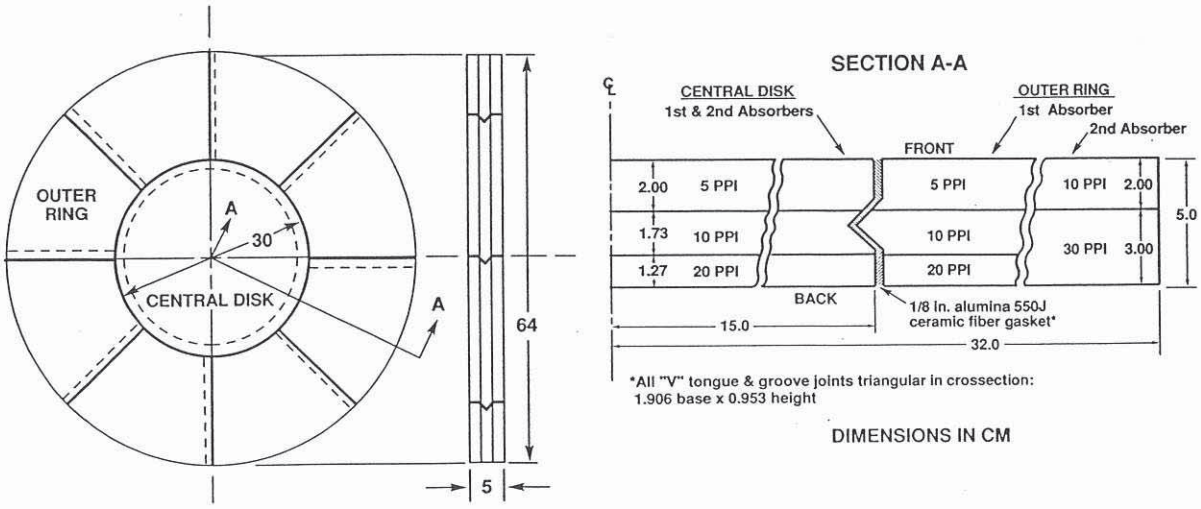


**Figure 2. Schematic of the CAESAR Absorber Inserts**

Two absorber inserts were installed during testing. The first insert had three axial layers and was radially uniform to provide a uniform mass flow through all zones. The second absorber was radially nonuniform, having the same inner disk as the first insert (with three axial layers) and an outer ring built of two axial layers of smaller pore size material to obtain higher

flow resistance and thus lower mass flow through these sections. This was used to adapt the local mass flow better to local solar irradiation. A schematic of the absorber inserts is given in Figure 2.

The properties of the various absorber layers were determined by SNL. For the radiative properties evaluation, small samples of reticulated foam were loaded with catalyst in a similar manner as done on the real absorber. Extinction coefficients and albedo were determined by measuring the hemispherical reflectance and transmittance with an integrating sphere. The data were spectrally weighted by the solar energy distribution (air mass 1.5) for the solar band and by the Planck distribution at 1300K for the infrared band. From the weighted reflectance and transmittance data for various thicknesses, the needed properties are determined with a two-flux model.

The specific convective heat transfer area was calculated by using optical image analysis and stereological relationships to relate measurable two-dimensional planar quantities to three-dimensional volumetric quantities. The convective heat transfer coefficient was estimated from correlations for flow through woven meshes and from correlations for flow past single cylinders.

The catalyst loading, expressed as % weight of rhodium, was determined on unused absorber pieces (spare pieces). Originally a rhodium loading of 0.2% weight was desired but the examination of the prepared absorber pieces showed great deviations from this value. After removing the first absorber insert, the catalytic activity of both used and unused pieces was determined showing significant deactivation of the catalyst.

The data sets used for the simulation runs are listed in the following sections for both absorber inserts.

### First Absorber Insert

The first absorber insert used the same layer configuration for the inner disk and the outer ring pieces (see Figure 2 on page 8). The front layer (i.e. the directly irradiated layer) was built of 5 PPI foam with a thickness of 20mm, the middle layer was 17.3mm of 10 PPI and the back layer was 12.7mm of 30 PPI. The radiative, thermodynamic and chemical properties are listed in Table 2.

| PPI number | $k_{t,S}$ (1/m) | $\omega_S$ (-) | $k_{t,IR}$ (1/m) | $\omega_{IR}$ (-) | $\Gamma$ (%) | $A_{cV}$ ($m^2/m^3$) | $h$ ($W/m^2K$) |
|---|---|---|---|---|---|---|---|
| 5 | 327.7 | 0.272 | 359.7 | 0.540 | 0.6 | 600 | 74 |
| 10 | 651 | 0.500 | 807 | 0.771 | 0.3 | 900 | 79 |
| 20 | 955 | 0.544 | 1152 | 0.803 | 0.4 | 1400 | 100 |

**Table 2. Foam Properties for First Absorber Insert**

### Second Absorber Insert

The second absorber insert had the inner disk with the same layer configuration as in the first insert. The outer ring pieces were built of a front layer of 10 PPI foam with a thickness of 20mm and a back layer of 30 PPI having a thickness of 30mm (see Figure 2 on page 8). This layout was chosen as a result of calculations performed by SNL to match the local mass flow better to the local irradiation by introducing two regions with different fluid velocities. Based on the assumption that the pressure drop over the inner disk and outer ring sections should be the same the mass flow ratio is about 3 (i.e. the inner disk has a local fluid velocity being three times the velocity of the outer ring sections). The calculations were based on an inlet

fluid composition with a $CO_2/CH_4$-ratio of 1.2 and an average temperature of 1000K. The radiative, thermodynamic and chemical properties for the outer ring pieces are listed in Table 3 on page 10.

| PPI number | $k_{t,S}$ (1/m) | $\omega_S$ (-) | $k_{t,IR}$ (1/m) | $\omega_{IR}$ (-) | $\Gamma$ (%) | $A_{eV}$ ($m^2/m^3$) | $h$ ($W/m^2K$) |
|---|---|---|---|---|---|---|---|
| 10 | 651 | 0.500 | 807 | 0.771 | 0.6 | 900 | 79 |
| 30 | 1560 | 0.577 | 1830 | 0.822 | 0.4 | 1800 | 120 |

**Table 3. Foam Properties for Outer Ring Pieces of Second Absorber Insert**

### Optical Properties of the Window

The optical properties of the window are based on technical information from the manufacturer and given in Table 1 on page 8. In the spectral range of solar radiation quartz has very little absorption, only in the UV and IR some absorption bands are existing. In the wavelength range $> 3\mu m$, quartz is opaque, having some bands with little reflection. The data used are based on a temperature-weighted evaluation of the spectrally dependent properties.

### 3.1.2 Operation Data

A number of tests were selected for comparison with the simulation model. The tests were selected by two criteria:

- test conditions (insolation, mass flow, exit composition) should be stable for a few minutes before the data was taken
- the solar flux distribution applicable to the test must be available (the corresponding HERMES-measurements must have been performed)

Following these criteria a total number of 8 test conditions were chosen for the simulation. Each specific case has an identifier of the form

**IX.YY;ZZZ**

with

**I** insert identifier (1 = first, 2 = second insert)

**X** one character: data acquisition table identifier

**YY** two digits (sometimes followed by a 'T'): test identifier

**ZZZ** one to three digits: actual test time (minutes)

An overview of the simulated test runs with some operation data and measured results is given in Table 4 on page 11.

Since the fluid exits directly through the flare into atmosphere with negligible pressure drop ($\Delta p < 1$mbar), the receiver pressure equals ambient pressure. This pressure ranged normally between 950 and 1000mbar.

The fluid inlet temperature is assumed to be 27°C. This is not exactly the temperature of the fluid entering the absorber, since the fluid then already passed the ring channel and the inlet section where partial heating occures. But no measurements were taken to determine the exact temperature, and therefore the above assumption was chosen.

| test identifier | feed: $\dot{n}_{CH4}$ (mol/s) | feed: $\dot{n}_{CO2}$ (mol/s) | ratio $CO_2/CH_4$ | $P_{inc}$ (kW) | $P_{sens}$ (kW) | $P_{reac}$ (kW) |
|---|---|---|---|---|---|---|
| 1L.34;40 | 0.5209 | 0.4746 | 1.098 | 105.7 | 30.2 | 53.6 |
| 1L.42;27 | 0.2007 | 0.1775 | 1.131 | 86.3 | 12.5 | 21.8 |
| 1L.44;25 | 0.1922 | 0.1719 | 1.118 | 78.7 | 11.8 | 22.4 |
| 1L.44;39 | 0.1312 | 0.1023 | 1.283 | 74.8 | 8.2 | 15.5 |
| 2C.07;18 | 0.3262 | 0.2974 | 1.097 | 75.0 | 19.0 | 38.0 |
| 2C.08T;90 | 0.2007 | 0.1775 | 1.131 | 64.1 | 13.5 | 29.7 |
| 2C.13T;40 | 0.2524 | 0.1873 | 1.348 | 72.1 | 15.2 | 32.3 |
| 2C.17T;60 | 0.3456 | 0.3302 | 1.047 | 97.3 | 22.8 | 44.1 |

**Table 4. CAESAR Tests Selected for Comparison with Simulation**

**Incident Solar Radiation**

The solar irradiation for the simulation runs is based on measurements taken with the HERMES system developed at DLR [9]. The measurements were taken under conditions as close as possible to the corresponding CAESAR test runs. This means that the focal distance and the position and number of cover sheets on the dish surface (if used) was identical to the corresponding CAESAR test. The output of a HERMES measurement is the solar flux density distribution in the receiver aperture plane, given with a spatial resolution of 256x256 pixels which corresponds to a rectangular area of 1.2m squared. With a special FORTRAN code, the averaged solar insolation on each receiver zone could be determined. For this purpose, it is assumed that the receiver center is located at the radiation center of the focal spot measured by HERMES (i.e. the intercept factor has its highest value). Thus, knowing the spatial distribution of solar flux and the position of the receiver relative to this distribution, it is possible to integrate the solar flux falling on each zone of the window (outer side) directly. To get the incident solar radiation on the absorber it is assumed that the radiation distribution doesn't change from the aperture area to the absorber area. This assumption is justified since the absorber plane is located only 3cm behind the window plane. This means that the direct solar irradiation on the absorber zones equals the irradiation onto the corresponding window zone (outer side) multiplied by the transmissivity of the window in the solar wavelength range. The inner window side zones and the ring gap (fluid inlet section) are assumed to be not irradiated by direct insolation.

Furthermore, it is assumed that the solar flux could be scaled directly with the level of insolation. This implies that the shape of the focal spot does not change with varying insolation (and varying sun shape). The calculated average on each zone was therefore scaled with the ratio between insolation apparent during the CAESAR test and insolation during the HERMES measurement. In addition the concentrated radiation is modeled as collimated irradiation with an incidence angle angle of 25.8° ($\mu$ = 0.9), which is a good approximation to the angular distribution ranging from 0 to 32° for the PAN dish.

As the result of the described procedure, all direct solar radiation data is available as input data for the simulation of a given test case. The diffuse parts of the solar radiation (diffuse reflections) are treated within the overall model and are not needed as input data. A representative flux distribution is shown in Figure 3 on page 12. Figure 4 on page 12 shows a vertical scan through the peak. This distribution is valid for the test case 2C.17T;60. The distribution shows rather steep gradients, which make it difficult to determine the flux incident on a specific zone.

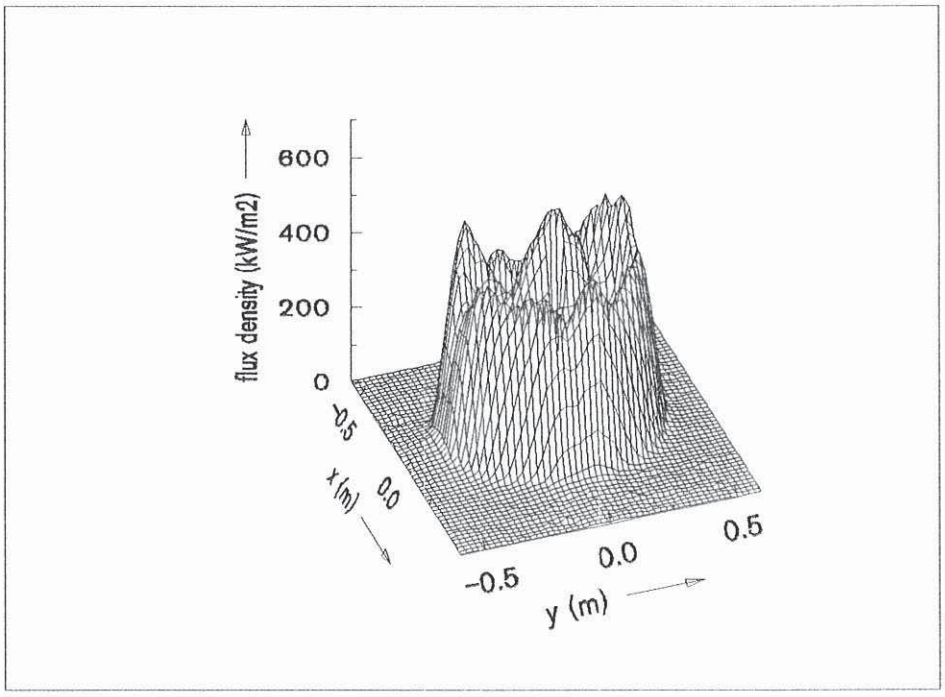


**Figure 3. Solar Flux Distribution for Case 2C.17T;60**

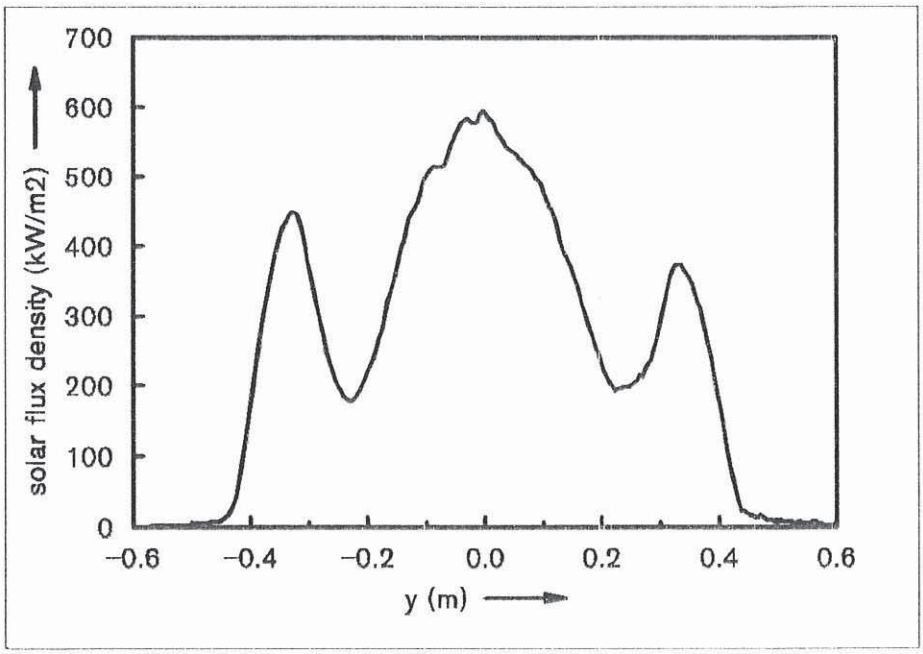


**Figure 4. Solar Flux Distribution for Case 2C.17T;60** (vertical scan through peak)

## 4. Results of CAESAR Simulation Runs

During the first simulation runs, the basic receiver data (as given in the previous sections) were taken without additional modification of parameters. The corresponding results for the selected cases are given in Table 5. The comparison is based on receiver and chemical efficiencies and on methane conversion which are defined as follows:

- receiver efficiency:

$$\eta_{rec} = \frac{\text{power absorbed as heat and by reactions}}{\text{solar radiation through aperture}} \tag{20}$$

- chemical efficiency:

$$\eta_{chem} = \frac{\text{power absorbed by reactions}}{\text{solar radiation through aperture}} \tag{21}$$

- methane conversion:

$$\chi_{CH4} = \frac{\text{amount of methane flow which is reformed}}{\text{total methane flow in feed gas}} \tag{22}$$

| test identifier | receiver efficiency test / model (diff.) (%) / (%) (%) | chemical efficiency test / model (diff.) (%) / (%) (%) | methane conversion test / model (diff.) (%) / (%) (%) |
|---|---|---|---|
| 1L.34;40 | 79.3 / 80.9 ( +1.6) | 50.7 / 52.0 ( +1.3) | 45.9 / 45.1 ( -0.8) |
| 1L.42;27 | 39.7 / 74.9 (+35.2) | 25.2 / 50.7 (+25.5) | 48.8 / 98.1 (+49.3) |
| 1L.44;25 | 43.4 / 76.0 (+32.6) | 28.5 / 52.7 (+24.2) | 51.6 / 96.1 (+44.5) |
| 1L.44;39 | 31.7 / 56.0 (+24.3) | 20.8 / 33.2 (+12.4) | 60.0 / 99.9 (+39.9) |
| 2C.07;18 | 76.1 / 75.3 ( -0.8) | 50.7 / 49.0 ( -1.7) | 50.9 / 48.2 ( -2.7) |
| 2C.08T;90 | 67.3 / 72.5 ( +5.2) | 46.3 / 49.4 ( +3.1) | 66.0 / 70.3 ( +4.3) |
| 2C.13T;40 | 65.9 / 72.2 ( +6.3) | 44.9 / 47.7 ( +2.8) | 68.5 / 71.5 ( +3.0) |
| 2C.17T;60 | 68.7 / 75.1 ( +6.4) | 45.3 / 50.4 ( +5.1) | 52.4 / 58.7 ( +6.3) |

**Table 5. Comparison between Test Data and Simulation Results** (in parenthesis: absolute difference)

Excluding the tests 1L.42 and 1L.44 (3 comparisons) the agreement between measurements and simulation is quite good. The absolute difference is

- for the receiver efficiency: $< 6.4\%$
- for the chemical efficiency: $< 5.1\%$
- for the methane conversion: $< 6.3\%$

The two excluded tests show extreme differences between test data and simulation. The reason for the poor agreement for these two tests is quite clear. During the test 1L.39, the RTV [1]) window sealing failed by partial decomposition. A white surface layer appeared on some regions of the absorber which was later determined to contain silicon (a main component of the RTV). This changed the optical properties (white spots increased the diffuse solar reflection losses) and could have affected the chemical activity of the catalyst, thus increasing absorber temperatures. Since it is not possible to account for these effects, all tests with the first absorber insert following 1L.39 (the window sealing failure) were omitted from further

[1]) RTV: room temperature vulcanisation

examination. The data for subsequent tests also indicate that the receiver behaviour changed drastically at that time. After installation of the second absorber insert (indicated by '2' as first digit of the test identifier), the agreement between simulation and tests is again quite acceptable.

Various temperature measurements were taken during the experiments. A set of thermocouples was installed in the inner disk within a radius of 2.5cm around the center of the absorber at different depths. Thus, some information about the axial temperature distribution was obtained. The temperature readings of these thermocouples are compared to theoretical values in the following sections. It is clear that without further correction these readings do not really represent the absorber temperatures because the energy transfer mechanisms at the thermocouple are quite different to those of the absorber. Radiative properties, chemical activity and heat transfer characteristics are poorly known and it is therefore a difficult task to perform a reasonable correction on these measurements. The thermocouple near the front is expected to be quite sensitive to direct solar irradiation (due to the high local intensity), whereas the thermocouples deeper in the absorber (> 2cm) are expected to be close to thermodynamic and chemical equilibrium thus reducing the measurement error (see for example Figure 5 on page 16: solid and fluid temperatures are quite the same at this depth, and remain nearly unchanged towards the rear side of the absorber). All thermocouples inside the absorber are type K elements and were originally believed to be chemically inert but local carbon deposition in the vicinity of the thermocouples showed that at least the carbon-forming reaction was catalyzed by the sheath material. No information was available about the activity for the reforming and watergas reactions. For the above reasons the thermocouple readings were not corrected, but the elements towards the rear of the absorber are believed to give reasonable measurements.

The comparison of absorber temperatures was performed for the remaining five test cases (as discussed above). In a first step, the measured values are plotted versus the temperature distribution which resulted from the receiver calculation for the inner disk. All data for the receiver calculation are averaged over the specific receiver element (i. e. over the inner disk). Thus, it is clear that the calculated numbers represent also some kind of average temperatures. Since the solar flux distribution is quite inhomogeneous and the peak is located near the center where the thermocouples are installed, it is expected that the agreement between measured and calculated temperatures could be poor. Nevertheless, the calculated data are included in the figures as '**inner disk**'.

To obtain more realistic data for the absorber center, additional calculations were performed. For this purpose a simpler receiver configuration was used consisting only of absorber, window (front and back side) and aperture. Interactions by other receiver sections were neglected. For the insolation the peak values as determined by the HERMES measurements in the center of the focal spot were used. This procedure led to somewhat higher temperatures thus reducing the discrepancy between measurements and calculations. These results are included in the figures as '**center temperatures**'.

Hogan et al. [8] proposed in their paper to decrease the chemical activity of the catalyst by a factor of 8 to improve the agreement between their calculations and the measurements. This proposal is based on the post-test evaluation of the first absorber which showed significant catalyst deactivation [5]. Runs were performed with the catalytic activity reduced to 1/8 the nominal value using the 'simplified' configuration to determine the center temperatures based on peak insolation level. These results are also included in the figures as '**center temperatures; reduced activity**'. They show drastically higher front temperatures which decrease rapidly to a level below the temperatures for the case with nominal catalytic activity. The reduced activity does not improve the agreement between measurements and calculation. Therefore, it is believed that the catalyst deactivation is not that severe as proposed. The measured catalyst deactivation represents the status after all tests and after the window sealing failure, and the assumption that the measured post-test activity is valid for the above tests is somewhat doubtful. The strong deactivation determined during the post-test evaluation might be explained by the window sealing failure which occured with the first absorber

insert. As stated above this failure created a drastic change in receiver performance which might be due to a reduction in catalyst activity. For the second absorber no activity measurements were available.

There exists another effect which might be very important for the temperature distribution of a volumetric absorber. The mass flow used in previous calculations was based on the assumption of homogeneous mass flux (mass flow per frontal area) for the first absorber insert and on two different but homogeneous mass fluxes in the inner and outer sections of the second absorber insert, respectively. This assumption holds under conditions with constant fluid properties, but with changes in composition and temperature it might be incorrect. The local mass flux depends on local pressure drop which is mainly determined by the fluid velocity. However, the fluid velocity changes due to

1. chemical reaction: the methane reforming reaction converts 1 mol of reactants to 2 mols of products thus doubling the fluid velocity.
2. temperature effect: fluid density decreases with higher temperatures thus increasing fluid velocity.

Both effects are accompanied by changes in viscous properties, but the influence of velocity is believed to be the major effect determining the pressure drop through the absorber [2]). The complete absorber could be understood as an assembly of many absorber sections connected in parallel which means that the pressure drop (the pressure difference between front and back side of the absorber) is the same for all sections. In those absorber zones having high local solar flux densities (i.e. the peak in the absorber center) both the fluid temperature and the reaction extent are higher compared to zones with lower solar fluxes. With the requirement that all zones should have the same pressure drop, it is clear that this could only be achieved by a locally decreased mass flux in the zones with high solar flux densities. However, this decrease in mass flux results in a further increase of local reaction extent and temperatures. This 'positive feedback' might introduce drastic local differences in mass flux. There were in fact some observations made during the tests which support the aforementioned effect. Shifting the focal spot relatively to the receiver position by a small distance (few centimeters) led in some tests to drastic changes in some temperature readings. For example, during the test 2C.86T at $t = 70$min the dish offset was changed, thus moving the focal spot a few centimeters. This resulted for the thermocouple SS8 (located at a radius of 10cm at the rear side of the absorber) in a temperature decrease from more than 1000°C to about 700°C. Further evaluation is necessary to determine the influence of changed irradiation and eventually local mass flow variations.

To evaluate the aforementioned effect, some calculation runs were performed for the center temperatures with the simplified model and the peak insolation data. Various mass flow reductions were tested for their influence on the axial temperature distribution. It was found that with a local mass flux reduction to 70% the nominal value for the inner disk the agreement between measurements and calculation could be improved significantly. These calculations are given in the figures indicated as '**center temperatures; reduced mass flow**'. Especially for the tests with the second absorber the measurements are quite close to the calculated temperatures indicating that the assumed effect might explain the thermocouple readings.

It will be hard to achieve better agreement between measurements and simulation due to the following uncertainties in the test data:

- the radiative properties of the absorber were determined on untested samples. It was therefore not possible to account for changes occuring during the tests.
- the chemical activity of the absorber was determined on untested samples and on tested samples of the first absorber after all experiments incl. window sealing failure. The

[2]) A report dealing with the pressure drop calculations is in preparation

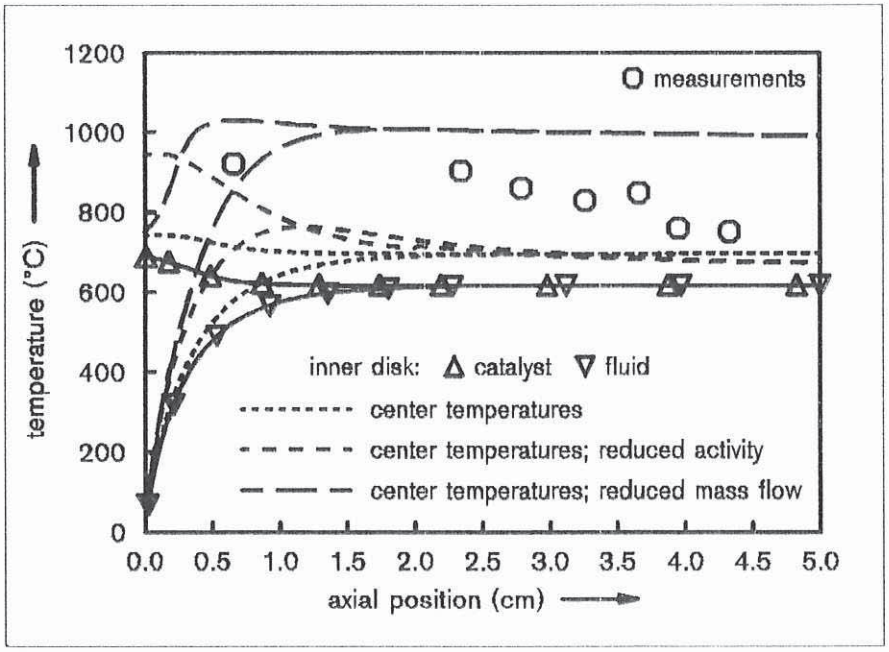


Figure 5. Comparison of Temperatures for Test 1L.34;40

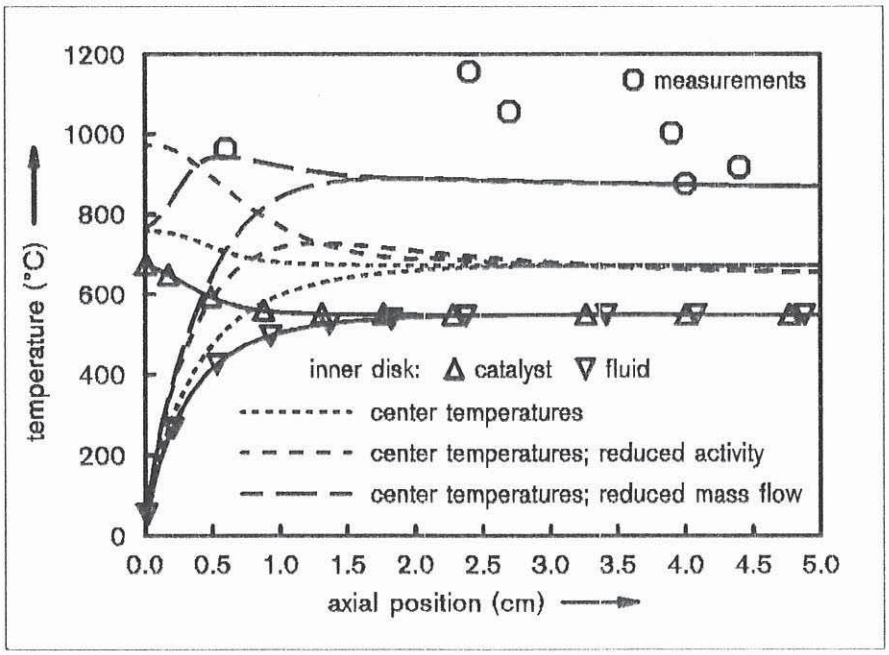


Figure 6. Comparison of Temperatures for Test 2C.07;18

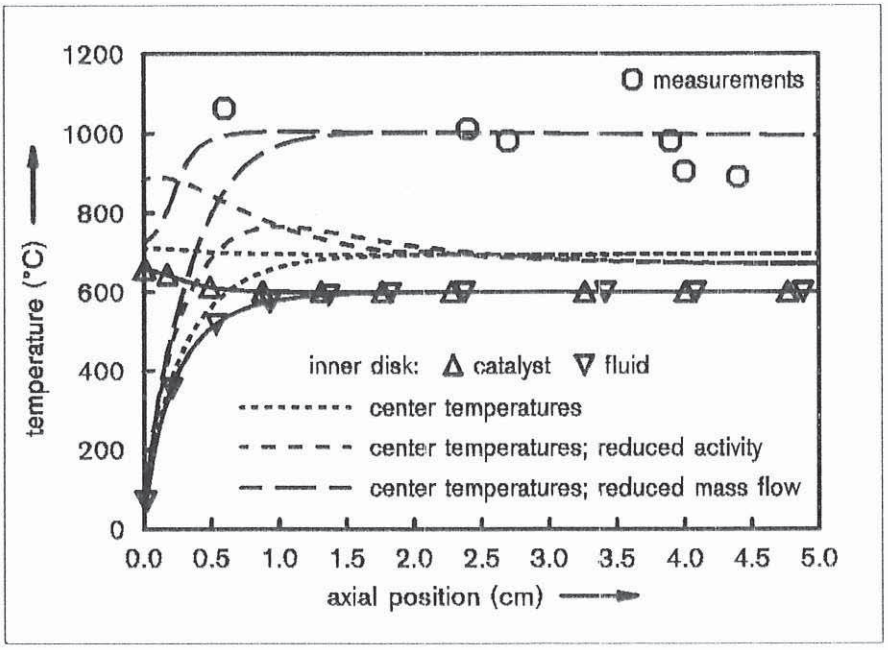


Figure 7. Comparison of Temperatures for Test 2C.08T;90

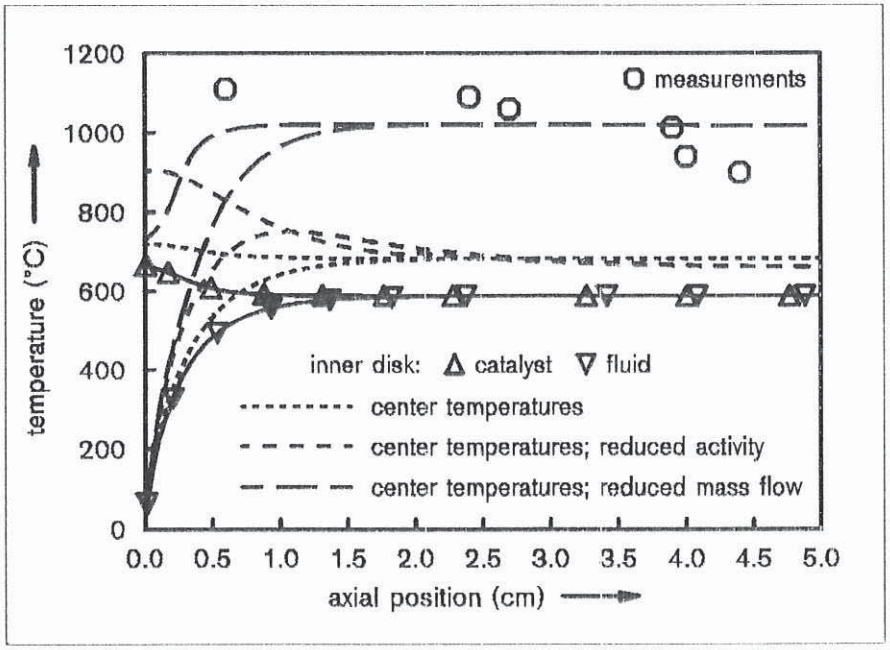


Figure 8. Comparison of Temperatures for Test 2C.13T;40

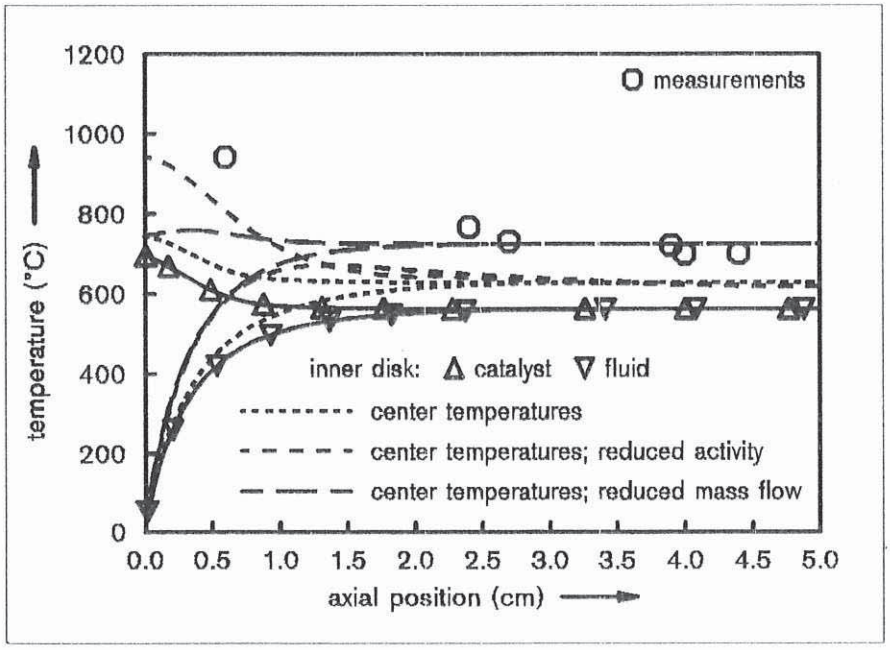


**Figure 9. Comparison of Temperatures for Test 2C.17T;60**

changes during testing (due to catalyst deactivation and sintering effects) have a great influence which results in a great uncertainty for the chemical reaction rates.

- the convective heat transfer was assumed to be independent on operation conditions which is obviously not true. But, as stated in 5.2.7 on page 35 this does not have a great influence on the results.
- the solar flux distribution was determined under somewhat different conditions. The altered weight distribution on the dish and different angular position of the sun might results in some elastic deformation of the receiver mounting with slight changes of focal distance. This as well as the influence of sunshape was neglected. Since both the test evaluation and the simulation were based on the same HERMES measurements the main difference remains the zone-averaged solar insolation for the receiver calculation.
- the assumed mass flow distribution was based on constant fluid properties. As stated above, local inhomogenities are expected due to changes in fluid composition and temperature which might increase with the local solar flux differences. The overall performance is not much affected by these local effects.

Most of these uncertainties can hardly be expressed by numbers without further detailed evaluation. Nevertheless, they might help in planning future experiments.

## Conclusions and Recommendations

The results of the receiver simulation showed quite good agreement in overall receiver performance. Despite some uncertainties in the input data used, the receiver and chemical efficiencies as well as the methane conversion were calculated close to the experimentally determined values. In general, the predicted values were slightly better (max. 6.4%) than the measured data. This is expected since the relatively coarse division of the receiver zones

implies the attenuation of the influence of locally inhomogeneous radiation and mass flow distribution.

The axial temperature distribution in the absorber center showed significant differences between measurements and simulation results. Two possible reasons were examined for their influence upon the temperatures. The assumption of reduced catalyst activity did not improve the agreement whereas the assumption of locally reduced mass flow resulted in much lower differences between measured and calculated temperatures. This effect of local mass flow reduction by changed fluid properties needs therefore more attention in future work. Further development of the simulation model will include pressure drop calculation and local mass flow adaption to evaluate this influence more exactly. A higher spatial resolution seems also necessary for this purpose. This could already be done with the current simulation model but the available data base with its great uncertainties did not justify this for the presented calculations.

## 5. Performance Studies

In order to identify the points where improvement is most promising, or to identify critical parameters, a variation for various parameters is performed. The 'base case' which serves as reference for comparison is described below.

### 5.1 Definition of Base Case

The base case model consists of a 5-zone receiver with a shape of a flat cylindrical disk. The description of the receiver zones is given in Table 6. The geometry for the model is similar to that of the CAESAR receiver-reactor, but no further division of absorber and quartz window was assumed. The absorber and window diameter are taken to be 600mm, the gap between the absorber and the window is 30mm. Window thickness is 10mm. The temperature of the ring wall zone is taken to be 627°C ( = 900K), the aperture ( = ambient) temperature is 27°C ( = 300K). Absorber and window temperatures are determined during the calculation. The runs were made with a two-band model for the radiative transfer, where the separation between the bands is at $3\mu m$. The first wavelength range (with shorter wavelengths) corresponds to solar radiation (index S), the second to thermal radiation (index IR). Of course, part of the thermal radiation is in the 'solar' band. The radiative properties of the window, the ring wall and the (imaginary) aperture are given in Table 7. Once again, the aperture (necessary to complete the enclosure) is assumed as black body absorbing all reradiation from the receiver. The exchange factors for this configuration are tabulated in A.2 on page 51.

| zone | area ($m^2$) | zone description |
|---|---|---|
| 1 | 0.2827 | catalytic absorber |
| 2 | 0.0565 | ring wall |
| 3 | 0.2827 | window, inner surface |
| 4 | 0.2827 | window, outer surface |
| 5 | 0.2827 | (imaginary) aperture |

**Table 6. Base Case: Receiver Zone Description**

| | $\alpha_S$ | $\alpha_{IR}$ | $\rho_{S,sp}$ | $\rho_{IR,sp}$ | $\rho_{S,dif}$ | $\rho_{IR,dif}$ |
|---|---|---|---|---|---|---|
| ring wall | 0.5 | 0.5 | 0.0 | 0.0 | 0.5 | 0.5 |
| window (quartz) | 0.02 | 0.95 | 0.08 | 0.05 | 0.0 | 0.0 |
| aperture | 1.0 | 1.0 | 0.0 | 0.0 | 0.0 | 0.0 |

**Table 7. Radiative Properties of the Receiver Elements**

The receiver is operated at a pressure of 1bar with an inlet fluid temperature of 27°C. The feed gas $CO_2/CH_4$ molar ratio is assumed to be 1.1. The incident solar radiation is collimated with an average incidence angle of 25.8° ($\mu = 0.9$), the flux density is 1MW/m².

The absorber is built from a catalytic ceramic foam absorber with 5 pores per inch (PPI 5). The thickness of the foam is 50mm, all other properties were taken to be identical to the data given in First Absorber Insert on page 9 (optical properties, convective heat transfer data etc.). The rhodium loading is 0.4% (weight). With a porosity of the reticulated foam absorber of 85%, the rhodium content is 0.025kg. The mass flow is chosen to give a methane conversion in the exit gas of 95%. The resulting mass flow is 0.0424kg/s. The fluid exit temperature is 832°C. If the fluid mixture were in chemical equilibrium, the resulting temperature for 95% methane conversion would be 807°C, indicating how far the exiting fluid mixture is from equilibrium. For the base case condition, this means that the temperature difference of

(832-807)°C could be used for further reaction (and therefore slightly higher conversion), if the exiting gas passes through another catalytic medium.

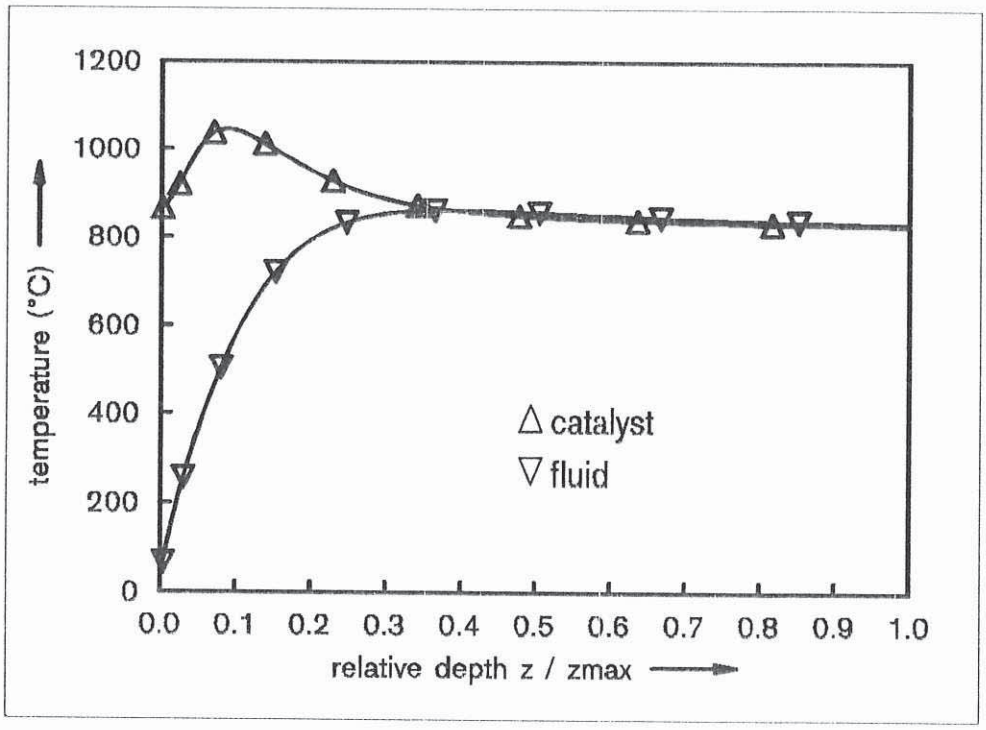


**Figure 10. Base Case: Absorber Temperature Profiles**

The resulting temperature profiles throughout the absorber are shown in Figure 10. Other results are:

- total incident power: $P_{inc}$ = 282.7kW
- receiver efficiency: $\eta_{rec}$ = 79.1%
- chemical efficiency: $\eta_{ch}$ = 55.7%
- power absorbed in sensible heat: $P_{sens}$ = 66.3kW
- power absorbed in chemical reactions: $P_{ch}$ = 157.6kW
- window temperatures: 710°C (outer surface), 795°C (inner surface)

The total loss in the base case can be subdivided into several loss mechanisms. These mechanisms are given in the following list, together with the numerical values of lost power (percentage of total incident power):

- reflection losses due to specular reflection from the window: 22.6kW (8.0%)
- reflection losses due to diffuse reflection of solar irradiation from the absorber: 12.4kW (4.4%)
- reradiation losses due to diffuse thermal emission from the receiver: 22.0kW (7.8%)
- other thermal losses: 2.1kW (0.7%)

The reflection losses mean that about 87.6% of the incident solar radiation is absorbed. This is the absolute maximum the receiver efficiency could reach for this configuration under any operation condition. Thermal losses, dependent on operating temperatures, lead to further reduction of the receiver efficiency.

Although the receiver geometry and operation conditions were chosen to be realistic (based on the experience with the CAESAR experiment and on information about current concentrator systems) this choice is somewhat arbitrary. For instance the catalyst loading and radiative properties were appropriate for the design phase of the CAESAR absorber. Therefore, these parameters could be improved by further research work. This should be kept in mind while interpreting the results of the performance study.

### 5.2 Parameter Variations

The parameter study should give information about the general behaviour of the volumetric receiver-reactor under varying operation conditions and about the influence of each parameter, thus identifying important or critical parameters. With the simple model used for this study (only one absorber zone with a flat geometry, one-dimensional), it is clear that these results only indicate trends, not absolute numbers. The parameters varied and the range of variation are

1. solar flux density (100 to 2000kW/m$^2$)
2. methane conversion (70 to 98%), by varying mass flow
3. catalyst activity (rhodium loading) (0.1 to 2.0 weight %)
4. absorber pore size (PPI 5 to PPI 30)
5. absorber porosity (85% and 92.5%)
6. radiative properties of the absorber ($0.0 \leq \omega \leq 0.5$)
7. convective heat transfer coefficient (10 to 500W/m$^2$K)
8. multiple layer absorber
9. inlet gas composition ($1.05 \leq CO_2/CH_4 \leq 1.5$)
10. operation with prereacted mixture
11. receiver pressure (0.5 to 10 bar)
12. heat exchanger efficiency (0 to 90%)

Most of the parameter variations were done with a methane conversion of 95% at the exit. This is achieved by setting the mass flow to a value which results in the desired methane conversion. This approach was taken because a certain conversion is the main purpose of such a receiver-reactor. In reality, this means that the control system of the plant will set the required mass flow (e.g. by adjusting blower speed).

#### 5.2.1 Solar Flux Density

Average solar flux density is varied from 100kW/m$^2$ to 2000kW/m$^2$, assuming homogeneous flux distribution on all receiver zones. On one hand, this reflects the influence of varying solar insolation (i.e. hazy / clear air conditions). On the other hand, information is obtained about a preferred operation regime for such a receiver. Two cases are considered, one with the exit methane conversion kept constant at 95% (and therefore varying mass flow), and the other with constant mass flow (and therefore varying methane conversion).

#### 5.2.1.1 Variation of Solar Flux Density with Constant Methane Conversion

For this variation, the exit methane conversion was kept constant at 95%. Figure 11 on page 23 shows the dependance of the efficiencies on solar flux density. There exists an optimum in the region of about 700kW/m², but this optimum is not very peaked.

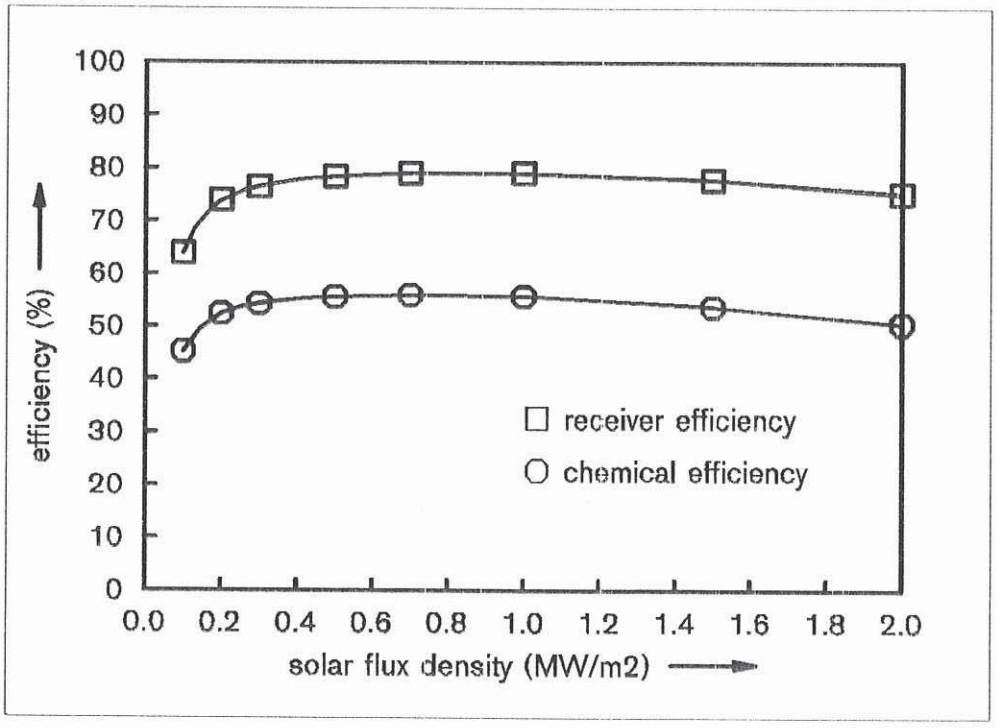


**Figure 11. Influence of Varying Solar Flux Densities on Efficiencies** (95% methane conversion)

Although the efficiencies are good even at relatively low flux densities, a sharp drop is apparent at flux densities less than 200kW/m². But even at 100kW/m², the efficiencies are pretty high compared to the outlet temperature necessary for the 95% methane conversion. The reason is the 'volumetric effect', which lowers temperatures in the front region ( = insolated region) of the absorber. This volumetric effect, as shown in Figure 12 on page 24 for a flux density of 100kW/m², results in front temperatures of the absorber (or catalyst) that are below the fluid exit temperature. Thus, the reradiation losses are significantly reduced at low solar flux densities which explains why the efficiencies remain quite high. The reduced front temperatures result from the improved ratio between rate-limited chemical energy transfer and mass flow. The mass flow decreases almost proportional to the solar flux density while the temperature-dependent reaction rates decrease less.
The temperature remains nearly constant for a relative depth greater than 0.2. This indicates that the fluid reaches equilibrium conditions in this region, from then on the composition and temperatures remain unchanged.

On the other hand, an increase in solar flux density results in a drastic increase of the absorber temperature in the front regions. The temperature profiles for a flux density of 2000kW/m² are also shown in Figure 12. The front region which is mainly responsible for the thermal reradiation losses, experiences very high temperatures, thus decreasing efficiencies. These high temperatures result from the limited reaction rates. These reaction rates, depending only on local catalyst temperature and local fluid composition, define the number of mols per time unit which are converted. The mass flow does not influence these rates. But

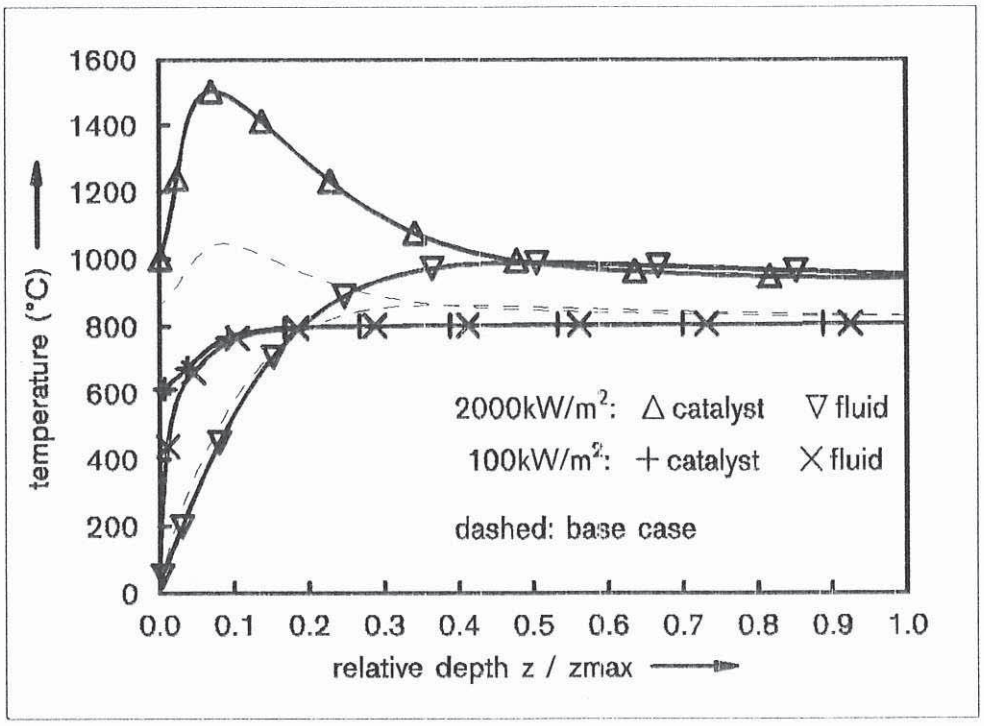


**Figure 12. Temperature Profiles at various solar flux densities** (95% methane conversion, temperature profiles of base case included for comparison)

a higher mass flow means that less percentage of the fluid is reacted (assuming negligible effect of fluid velocity on fluid mixing and adsorption on the catalyst). To increase the reaction extent (and the amount of energy transferred into the fluid) an increase in temperature is necessary (resulting in higher radiative losses). For the high flux case, the mass flow rate is 0.077kg/s (compared to 0.0036kg/s at 100kW/m²) imposing high catalyst temperatures to give the desired percentage conversion of methane. It could also be seen from the temperature profile that in the back region of the absorber the reaction isn't fast enough to convert the excess heat into chemical reaction, i.e. the fluid is far from chemical equilibrium at the absorber exit (the exit temperature is significantly higher than 807°C which is the equilibrium temperature for the specified 95% conversion).

The benefit of higher solar flux density in the receiver aperture is partially offset by the above mentioned thermodynamic flow effects, and therefore the influence on the efficiencies is not very pronounced. On the other hand, the temperature limitations of the support material and the catalyst must be regarded. This means that operation at flux densities between 400 and 1000kW/m² might be more advantageous in terms of material longevity without loss of efficiency.

### 5.2.1.2 Variation with Constant Mass Flow

During this variation the mass flow was kept constant at the base case value of 0.0424kg/s. As shown in Figure 13 the methane conversion increases almost linearly with solar flux density, with an offset of approximately 100kW/m². This offset is created by the fact that the reaction doesn't start until a certain temperature of the catalyst is reached (about 500°C). At solar flux densities above 1MW/m² the methane conversion is nearly completed with the consequence that no more energy could be absorbed by chemical reaction. Therefore, any

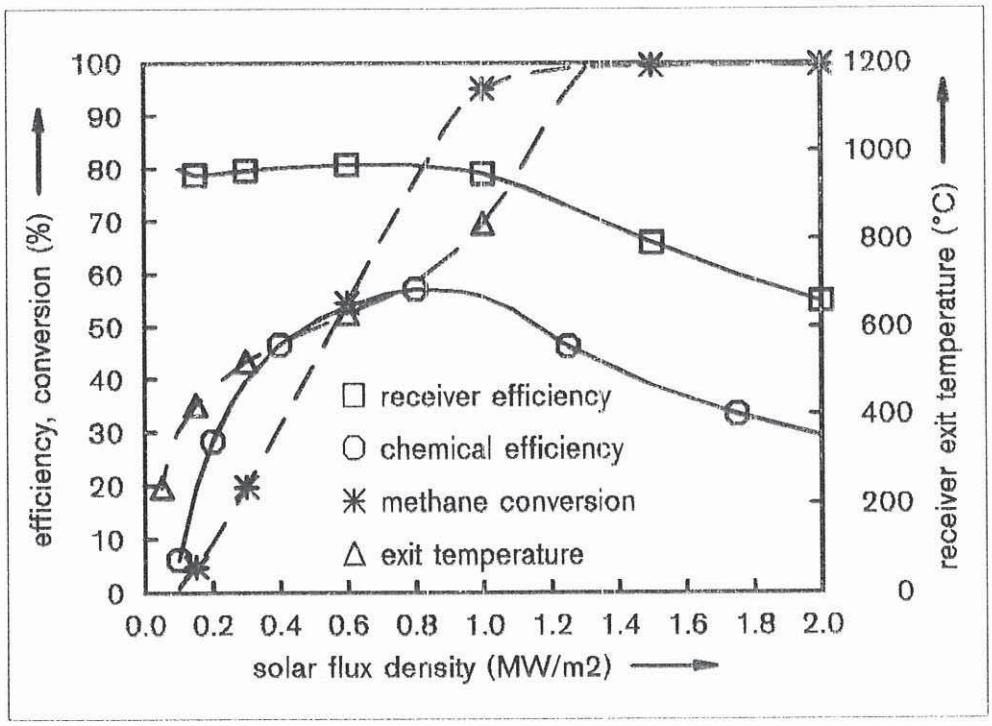


**Figure 13. Influence of Varying Solar Flux Densities on Efficiencies** (mass flow = 0.0424kg/s)

additional energy must be converted to sensible heat or must be offset by increased losses. Both effects result in a rapid increase of absorber temperature, higher reradiation losses, and thus lower efficiencies. It is obvious that the chemical efficiency has a pronounced peak in the region of 90 to 95% methane conversion, corresponding to solar flux densities of about $1MW/m^2$ in this specific case (for this mass flow). At lower flux densities the sensible heat fraction is increased with decreased methane conversion. On the other hand higher flux densities lead to an increase in thermal reradiation losses and therefore lower efficiencies.

These results indicate that the choice of the operation regime should be done very carefully. Since the desired methane conversion is normally above 90% the system needs proper mass flow control to prevent material overheating which can occur when the mass flow is too low compared to the solar flux density.

### 5.2.2 Methane Conversion

The overall methane conversion is one of the main design parameters of such a chemical receiver system. To identify the influence the methane conversion was varied between 70 and 98%. This is achieved by the variation of mass flow through the receiver while keeping solar flux density constant ($1MW/m^2$). The results are plotted in Figure 14. The influence of methane conversion on the efficiencies is not very pronounced except for very high conversion levels. As indicated in 5.2.1.2 on page 24 the absorber temperature and the reradiation losses increase drastically when the reforming reaction is nearly completed. This explains the decrease both in receiver and chemical efficiency.

The corresponding temperature profiles for the extreme cases of this variation are shown in Figure 15. Two effects should be considered. First, the equilibrium temperature is a function of exit methane conversion. Since the exit temperature tends to approach the equilibrium

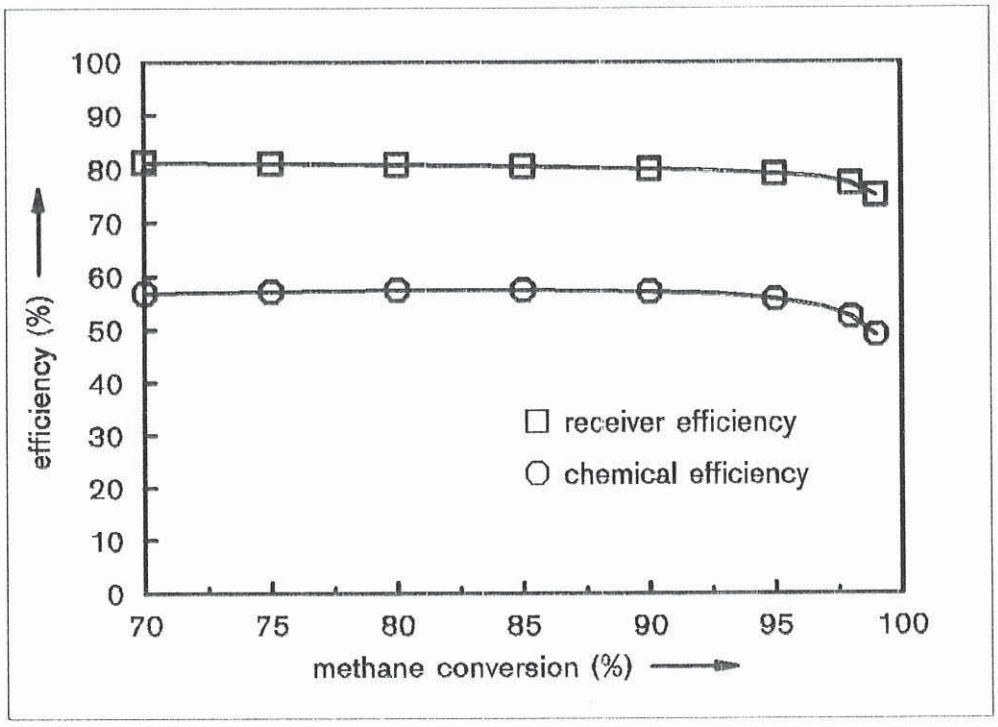


**Figure 14. Influence of Methane Conversion on Efficiencies**

status this explains the different temperature levels at the absorber exit ($z = z_{max}$). Another surprising result is that the absorber temperature at the front end ($z = 0$) remains nearly unaffected by varying exit conversion. This once again indicates that the temperatures are dominated by the local chemical reaction rates which are independent on mass flow but strongly dependent on fluid composition (which is fixed at the inlet). Throughout the receiver the change in fluid composition is different for each mass flow (and exit conversion) with the result of different temperature profiles inside the absorber.

From these results it could be concluded that the choice of the exit methane conversion is relatively insensitive in terms of efficiencies unless the conversion level doesn't exceed 95%. Another aspect of concern is the maximum material temperature which increases rapidly with high conversion levels.

### 5.2.3 Activity of the Catalyst

The performance of the catalyst directly influences the main energy transfer mechanism in a volumetric receiver-reactor, the chemical reaction. High catalytic activity, therefore, results in reduced absorber temperature, or vice versa. The catalytic activity depends on many factors. The catalyst loading (in weight%) is an important figure, but in reality, other effects might be even more important. Some of them are

- catalyst cristalyte size
- microporosity of the support structure
- dispersion of the catalyst
- sintering effects of the catalyst cristalytes and the support material

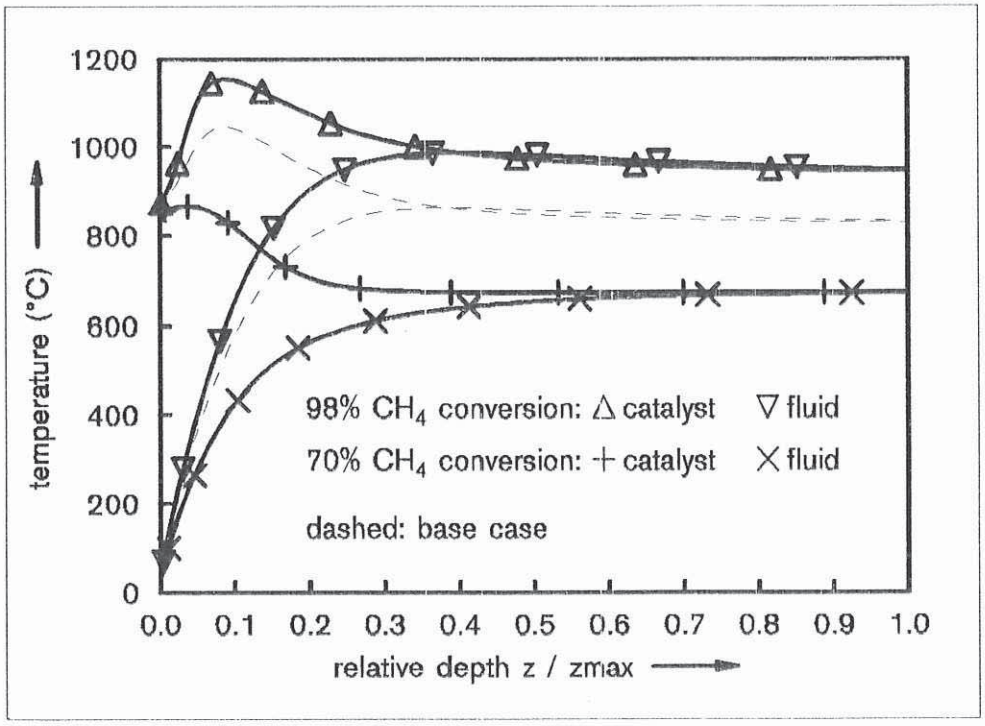


**Figure 15. Temperature Profiles for Various Methane Conversions** (temperature profiles of base case for comparison)

- deactivation of the catalyst (i.e. due to coating or poisoning)

To investigate the influence of catalytic activity, it was assumed that all these effects could be represented with the catalyst loading. The catalyst loading was varied from 0.1 to 2.0 weight % (base case loading is 0.4%).

Figure 16 shows the influence on the efficiencies when the mass flow is adapted to maintain the 95% methane conversion. At a catalyst loadings less than 0.4% both efficiencies begin to drop significantly, while there is no significant influence for higher loadings. The reason for this behaviour is easily understood from Figure 17 on page 29. Using a high catalyst loading reduces absorber temperatures and thereby radiative losses. In addition (not shown here) the exit composition is close to chemical equilibrium, with no excess heat. On the other hand low catalyst loadings create higher absorber temperatures (with higher reradition losses) and the exit composition is far from chemical equilibrium (due to the lack of catalyst to convert sensible heat into chemical reaction as fast as required). The latter means a lower feed gas mass flow to achieve the 95% methane conversion goal, increased temperatures and decreased efficiencies. For the given example the mass flow ranged from 0.0294kg/s (at 0.1% loading) to 0.0449kg/s (at 2.0% loading).

The efficiencies shown in Figure 16 with the drop beginning at 0.4% loading) are valid for the solar flux density of 1000kW/m². For higher flux densities this drop in efficiency tends to start at higher loadings, or vice versa.

From this data, it could be derived that the catalytic activity is a key parameter that affects both temperatures and efficiencies. To get (and to keep) the activity high must be a major issue in future developments. Furthermore, the proper selection of the catalyst loading is clearly dependent on the operation conditions. A higher loading doesn't necessarily mean

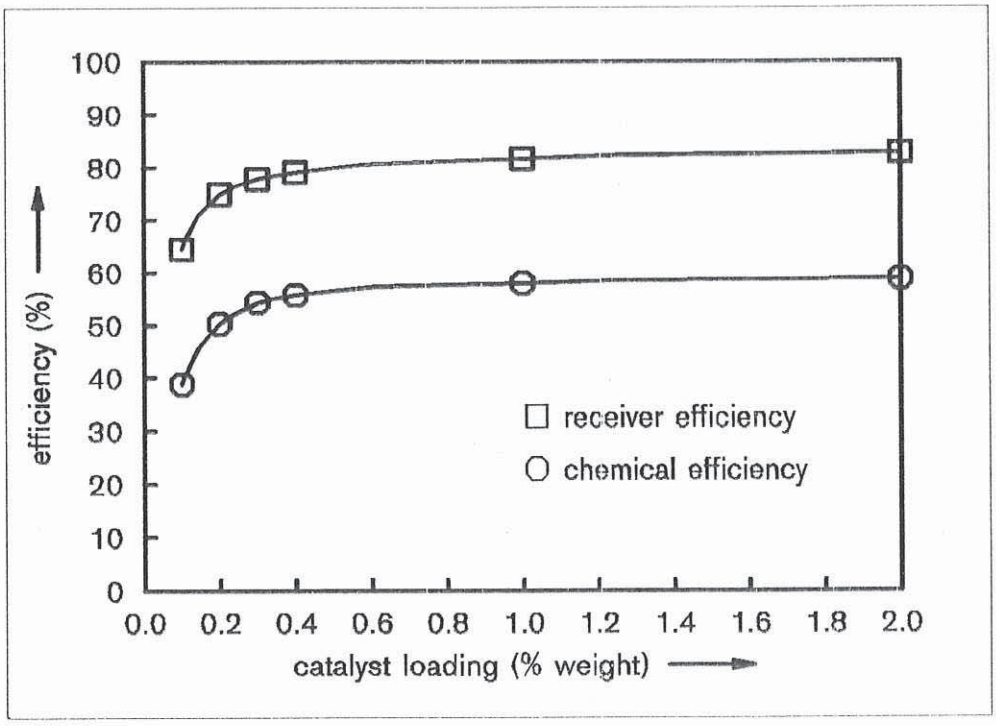


**Figure 16. Influence of Catalyst Loading on Efficiencies**

better performance and with the catalyst being one of the major cost factors, a careful determination of the catalyst loading is essential for an economic receiver design.

### 5.2.4 Absorber Pore Size

The proper selection of the absorber structure is one of the key elements in absorber design for volumetric receivers. For reticulated ceramic foams the pore size and the porosity (or bulk density) are the most important characteristics defining the macrostructure of the substrate. The pore size is defined by the PPI-number ( = *P*ores *P*er *I*nch). Of course, the above factors also influence the microstructure of the absorber (wash coat, active surface, microporosity etc.). Two cases are considered:

a) absorber characteristics based on the data determined during the CAESAR absorber evaluation

b) estimated absorber characteristics based on theoretical correlations

This distinction seems reasonable because it turned out that important characteristics of the CAESAR absorber (i.e. optical properties, catalyst loading) were strongly influenced by manufacturing and catalyst loading procedures.

#### 5.2.4.1 Variation Based on 'As Measured' Data

The relevant characteristics are based on the data derived for the CAESAR experiment with catalyst-coated foams of various PPI-numbers. The radiative and convective data were identical to the numbers given in 3.1.1 on page 7. The pore sizes considered range from PPI 5 to PPI 30, as used in the CAESAR absorber segments. The thickness of the absorber was kept constant at z = 50mm. The varying radiative properties result in a change in optical

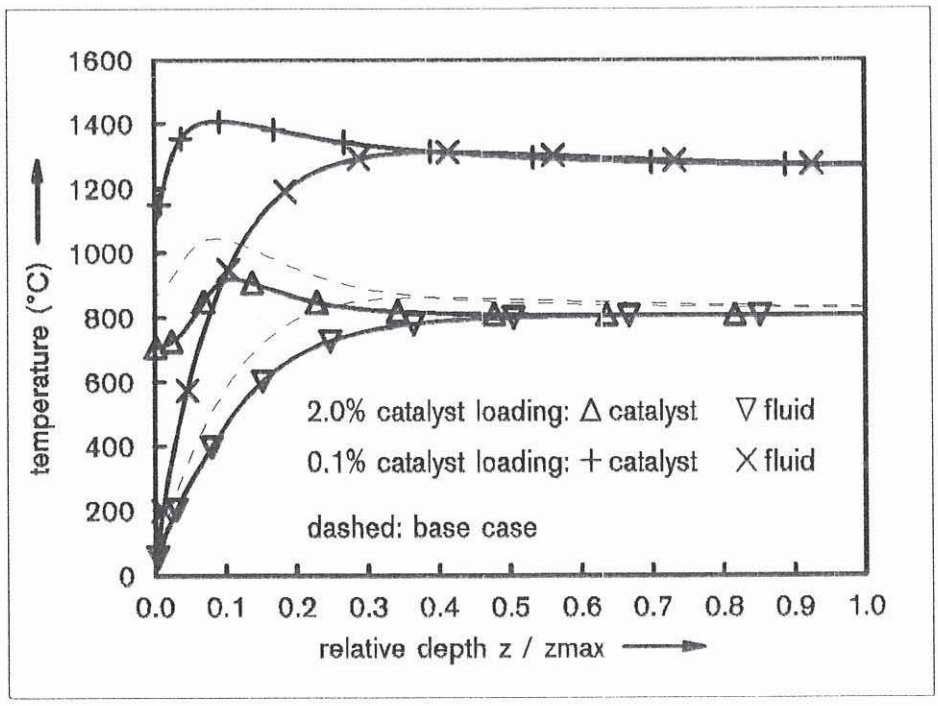


**Figure 17. Temperature Profiles for various Catalyst Loadings** (temperature profiles of base case for comparison)

depth of the absorber structure. The catalytic activity, given by the catalyst loading, was 0.4% weight (identical to the base case). The results of varying the PPI-number are given in Table 8 on page 29. The results show a decreasing efficiency (both receiver and chemical) with increasing PPI-number. The reasons for this behaviour are manifold. The penetration depth of the solar radiation, defined mainly by the extinction coefficients, decreases with smaller pore sizes (= higher PPI-numbers). Therefore, the amount of absorbed radiation energy per depth is increased. To convert more energy needs higher temperatures which occur especially in the frontal region of the absorber. Therefore, the peak of the temperature profile is shifted towards the front side of the absorber and the peak temperature increases. This is shown in Figure 18 on page 30. Both effects increase thermal reradiation losses with the consequence of lower efficiencies.

| PPI number | $\eta_{rec}$ (%) | $\eta_{ch}$ (%) | solar albedo |
|---|---|---|---|
| 5 | 79.1 | 55.7 | 0.272 |
| 10 | 71.9 | 50.7 | 0.500 |
| 20 | 70.4 | 49.7 | 0.544 |
| 30 | 67.3 | 47.8 | 0.577 |

**Table 8. Influence of PPI number on Efficiencies** (constant absorber thickness)

Another factor is the albedo of the foam material. Since the albedo in the solar band defines the diffuse solar reflection losses, there is a pronounced impact on efficiency. As pointed out

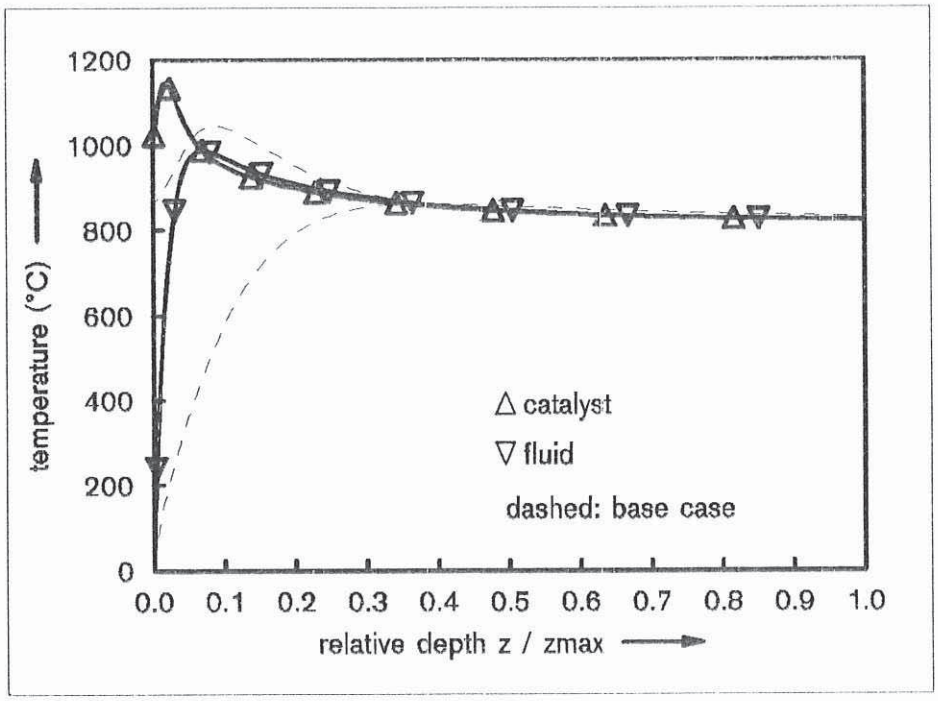


**Figure 18. Temperature Profiles for PPI 30 absorber (Constant Absorber Thickness)** (temperature profiles of base case for comparison)

in Table 8, the albedo determined during the CAESAR experiments is extremly different for the foams with PPI-numbers 10, 20 and 30 compared to the base case material which is PPI 5. As discussed in 5.2.6 on page 34, the higher albedo contributes to the total losses and therefore also decreases efficiencies. For this reason, it is difficult to identify the influence of pore size independent on other properties from this variation. To obtain more information, another variation was performed with theoretically estimated properties.

#### 5.2.4.2 Variation with Theoretically Estimated Properties

To evaluate the potential of ceramic foam absorbers with various PPI-numbers (neglecting not fully developed manufacturing and catalyst loading procedures), an attempt was done to estimate the 'theoretical' correlations of the foam material. The basic correlations to determine the properties theoretically are given in A.3 on page 52. The base case properties are used as reference values. The corresponding numbers are marked by the index 'ref'. All other values are varied as derived in the above mentioned section. These correlations in dependance of the PPI-number are summarized below. The absorber porosity (or bulk density) was assumed to remain constant.

Using (43) the convective heat transfer area per unit volume (identical to the specific surface area per unit volume) is

$$A_{cV,PPI} = A_{cV,ref} \cdot \frac{n_{PPI}}{n_{PPI,ref}} \tag{23}$$

As discussed in A.3 the catalyst loading $\Gamma$ (% weight) is also directly proportional to the specific surface area per unit volume (assuming a uniform catalyst distribution)

$$\Gamma_{PPI} = \Gamma_{ref} \cdot \frac{n_{PPI}}{n_{PPI,ref}} \tag{24}$$

The extinction coefficient changes according to equation (58) as follows:

$$k_{t,PPI} = k_{t,ref} \cdot \frac{n_{PPI}}{n_{PPI,ref}} \tag{25}$$

It was furthermore assumed that the albedo in the solar and infrared band is 0.272 and 0.54, respectively (identical to the base case). The extinction coefficients are calculated for both wavelength ranges. The convective heat transfer coefficient was assumed constant with 74W/m²K, although it is expected that this value increases with increasing PPI-number. The optical depth of the base case absorber is

$$\tau_{bc} = k_t \cdot z_{bc} \tag{26}$$

With the radiative properties and the thickness of the base case absorber the numerical value is $\tau_{bc} = 16.39$ The thickness of the absorbers with other PPI-numbers was adapted to the same optical depth. This approach is taken to get comparable results in terms of absorption characteristics. As stated in 5.2.4.1 there is no sense in using absorbers with different PPI-numbers without adaption of the thickness to obtain comparable radiation penetration.

The considered pore sizes ranged from PPI 5 to PPI 30, as used in the CAESAR absorber segments. The resultant numbers are listed in Table 9.

| PPI number | $k_t$ solar (1/m) | $k_t$ infrared (1/m) | $A_{cV}$ (m²) | catalyst loading (% weight) | absorber depth (cm) |
|---|---|---|---|---|---|
| 5 | 327.7 | 359.7 | 600 | 0.4 | 5.00 |
| 10 | 655.4 | 719.4 | 1200 | 0.8 | 2.50 |
| 20 | 1311 | 1439 | 2400 | 1.6 | 1.25 |
| 30 | 1966 | 2158 | 3600 | 2.4 | 0.83 |

**Table 9. Estimated properties for various PPI-number foams**

Performing the calculations leads to exactly the same results for all cases. The receiver efficiency is 79.1% whereas the chemical efficiency is 55.7%. The results indicate no influence of the pore size. Following the governing equations in the simulation model this behaviour has to be expected since it means only a scaling with absorber depth of the complete energy transfer problem.

From these results it could be concluded that there is no principal advantage for smaller or bigger pore sizes. If the theoretically predicted behaviour of the absorber properties could be reached in practice is a problem of manufacture development. Further research is necessary to examine and confirm these aspects.

### 5.2.5 Porosity of the Absorber

First the distinction between porosity and pore size of a porous medium should be made clear. Whereas the pore size is related to the geometrical dimensions of a single pore, the (macroscopic) porosity is defined by the ratio of two masses (see (41) on page 53). Varying the porosity while keeping the pore size (defined by the PPI-number) constant could be imagined as a variation of strut thickness. Thick struts lead to small porosities or vice versa.

The base case absorber material has a porosity of 85% (as used in the CAESAR experiment). For comparison an absorber having a porosity of 92.5% is considered. Both absorbers are

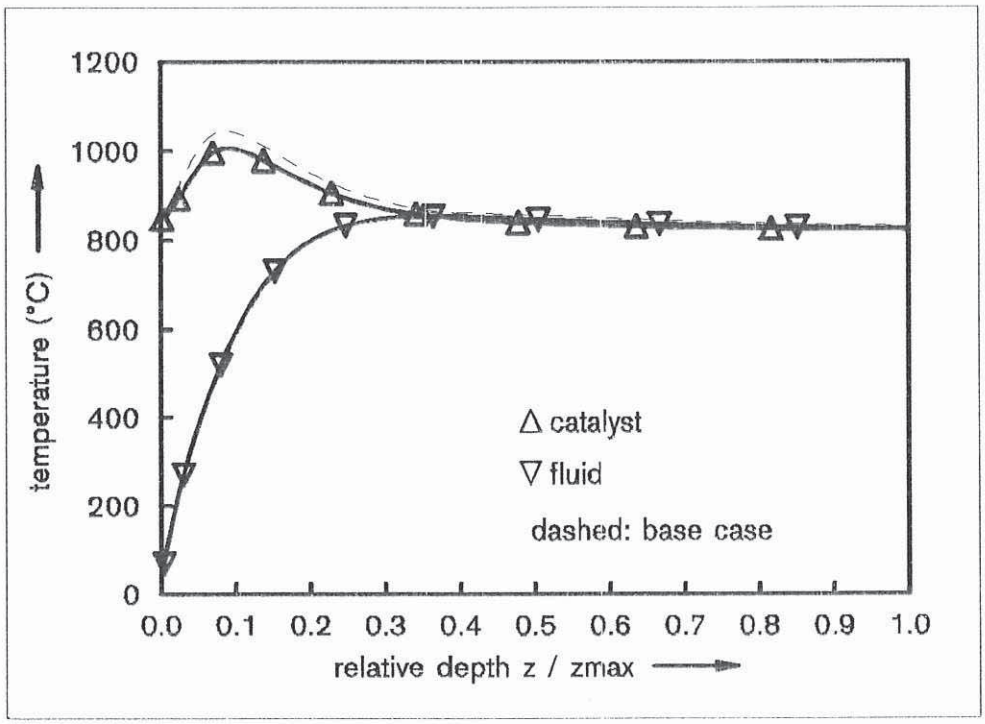


**Figure 19. Temperature Profiles for PPI 5 absorber (Varied Porosity)** (temperature profiles of base case for comparison)

assumed to have the same pore size (PPI 5). The properties were derived following the theoretical correlations in A.3 because no measured values are available.

Using the definition of the porosity (see (41)) it is obvious that the above increase in porosity is equivalent to

$$\rho_{bulk} = 0.5 \cdot \rho_{bulk,ref} \tag{27}$$

With (40) the ratio between the two densities could be expressed as

$$\frac{\rho_{bulk}}{\rho_{bulk,ref}} = \frac{\left(\frac{d}{s}\right)^2}{\left(\frac{d}{s}\right)^2_{ref}} \tag{28}$$

Combining both equations (with $s$ being constant for a constant pore size) results in

$$d = \sqrt{0.5} \cdot d_{ref} \tag{29}$$

With (43) the convective heat transfer area per unit volume (identical to the specific surface area per unit volume) is

$$A_{cV} = A_{cV,ref} \cdot \frac{d}{d_{ref}} \tag{30}$$

Following (45) the catalyst loading $\Gamma$ (% weight) for a varied porosity is estimated by

$$\Gamma = \Gamma_{ref} \cdot \frac{(\frac{d}{s})_{ref}}{(\frac{d}{s})} \tag{31}$$

From equation (40) the ratio d/s could be determined as 0.2523 for the reference porosity and as 0.1784 for $\psi = 92.5\%$. The extinction coefficient could then be calculated with equation (58):

$$k_t = k_{t,ref} \cdot \frac{\ln(1 - 2 \cdot \frac{d}{s})}{\ln(1 - 2 \cdot (\frac{d}{s})_{ref})} \tag{32}$$

As in the previous chapter the measured values of the base case absorber were taken as reference to determine the needed data. The albedo in the solar and infrared band is 0.272 and 0.54, respectively (identical to the base case). The extinction coefficients are calculated for both wavelength ranges. The convective heat transfer coefficient is assumed constant with 74W/m²K, although it is expected that this value increases with higher porosities (and therefore thinner struts). The absorber depth was also adapted to an optical depth of 16.39. The calculated properties are listed in Table 10.

| porosity (%) | $k_t$ solar (1/m) | $k_t$ infrared (1/m) | $A_{cV}$ (m²) | catalyst loading (% weight) | absorber depth (cm) |
|---|---|---|---|---|---|
| 85 | 327.7 | 359.7 | 600 | 0.4 | 5.00 |
| 92.5 | 205.9 | 226.0 | 424.3 | 0.566 | 7.96 |

**Table 10. Properties for Various Porosities (all PPI 5)** (estimated for 92.5% porosity)

| porosity (%) | $\eta_{rec}$ (%) | $\eta_{ch}$ (%) | $m_{cat}$ (gram) |
|---|---|---|---|
| 85 | 79.1 | 55.7 | 25.5 |
| 92.5 | 79.8 | 56.4 | 28.7 |
| <92.5> | <79.4> | <55.9> | <25.5> |

**Table 11. Influence of Porosity on Efficiencies** numbers in 〈 〉 with adapted catalyst loading

The calculated efficiencies are listed in Table 11. The results show very little influence of the porosity. The higher porosity absorber shows slightly improved efficiencies which could be explained by reduced temperatures in the front region of the absorber, as shown in Figure 19 on page 32. It should be noted that the x-axis shows the relative depth whereas the absolute depth is different in both cases. Except for the temperature peak in this region the catalyst temperatures are very similar. The decrease in catalyst peak temperature is partially related to the higher catalyst loading which improves the reaction kinetics. The total mass of catalyst deposited on the support structure ($m_{cat}$) is also slightly higher in this case (see Table 11). This is a result of the interrelations of varied absorber depth, porosity and catalyst loading. In terms of economic use of the expensive catalyst another calculation was performed with the total catalyst mass kept at the same value as in the base case. The corresponding results are included in Table 11 in parenthesis. Here once again the efficiencies are higher, but the difference is negligible. From these results higher porosities seem to have

relatively small advantages. The effect of improved convective heat transfer was excluded here. This effect, created by thinner struts in higher porosity structures, might give additional benefits.

### 5.2.6 Radiative Properties of the Absorber (Albedo)

The radiative properties (i.e. absorption and scattering coefficients) of the absorber matrix are defining the radiative exchange inside the absorber and might therefore have a big influence on the overall behaviour of the receiver. To verify the sensitivity of the losses to changes in these properties, the albedo of the absorber was varied. The total extinction (the sum of absorption and scattering coefficients) was kept constant. The albedo, defined as

$$\omega = \frac{k_s}{(k_a + k_s)} \tag{33}$$

was varied between 0.0 and 0.5 (equally for both wavelength bands), while keeping the total extinction coefficient constant. The albedo for the base case is 0.272 (in the solar band).

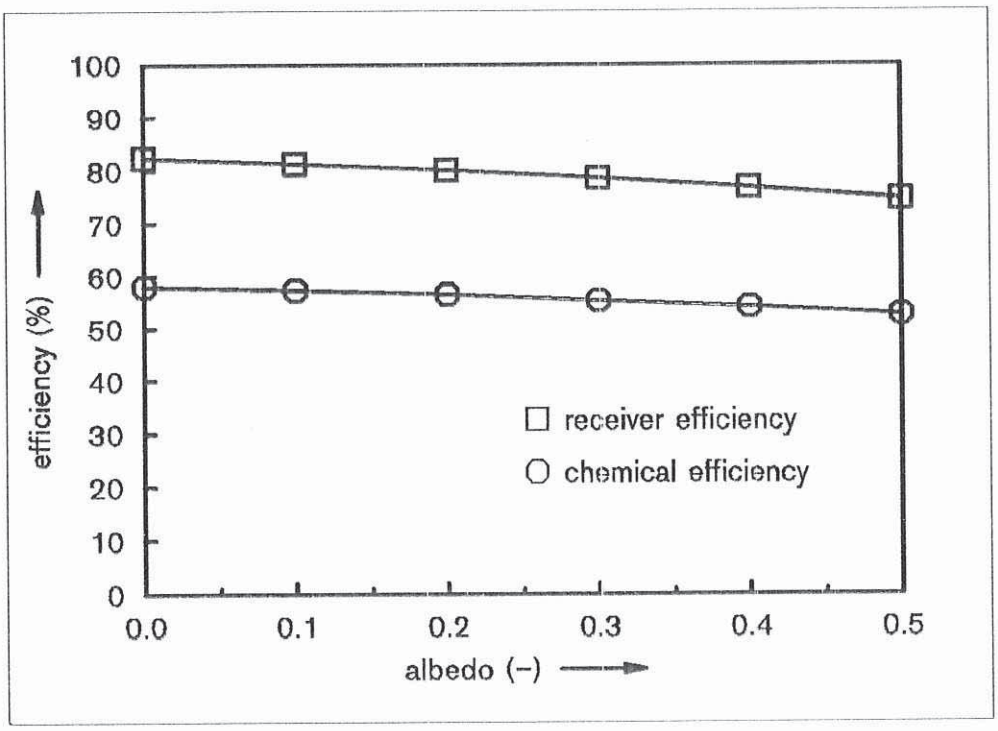


**Figure 20. Influence of Albedo on Efficiencies**

The main influence of the solar albedo is on the reflection losses in the solar band. An albedo of 0.0 means that no scattering is present, therefore no solar radiation is reflected back from the absorber. On the other hand a higher albedo means more radiation is scattered back from the absorber and is then mainly lost through the aperture. The amount of this reflection loss is tabulated in Table 12 on page 35 in absolute and percentage numbers. The diffuse reflection loss means here the diffuse solar reradiation leaving the aperture, taking into account the effect of multiple reflections of rays on absorber and window but excluding the first (specular) reflection on the window before hitting the absorber. As mentioned before, this specular reflection loss has a magnitude of 22.6kW (or 8% of the incident solar radiation).

| albedo (-) | reflection loss (kW) | reflection loss (%) |
|---|---|---|
| 0.0 | 0.00 | 0.00 |
| 0.1 | 4.05 | 1.43 |
| 0.2 | 8.67 | 3.10 |
| 0.272 | 12.4 | 4.39 |
| 0.3 | 14.0 | 4.95 |
| 0.4 | 20.3 | 7.18 |
| 0.5 | 27.9 | 9.87 |

**Table 12. Diffuse Solar Reflection Losses for Various Albedos**

Figure 20 shows the influence of varied albedo on efficiencies. As expected the solar losses increase with increasing albedo. Of interest is how strongly these losses depend on albedo. With the scattering coefficient equal to the absorption coefficient (albedo = 0.5) the losses increase by about 10% compared to an ideal absorber with no scattering. It should be kept in mind that the absorber is assumed to scatter isotropically (i.e. forward and backward scatter fractions are equal).

### 5.2.7 Convective Heat Transfer Coefficient

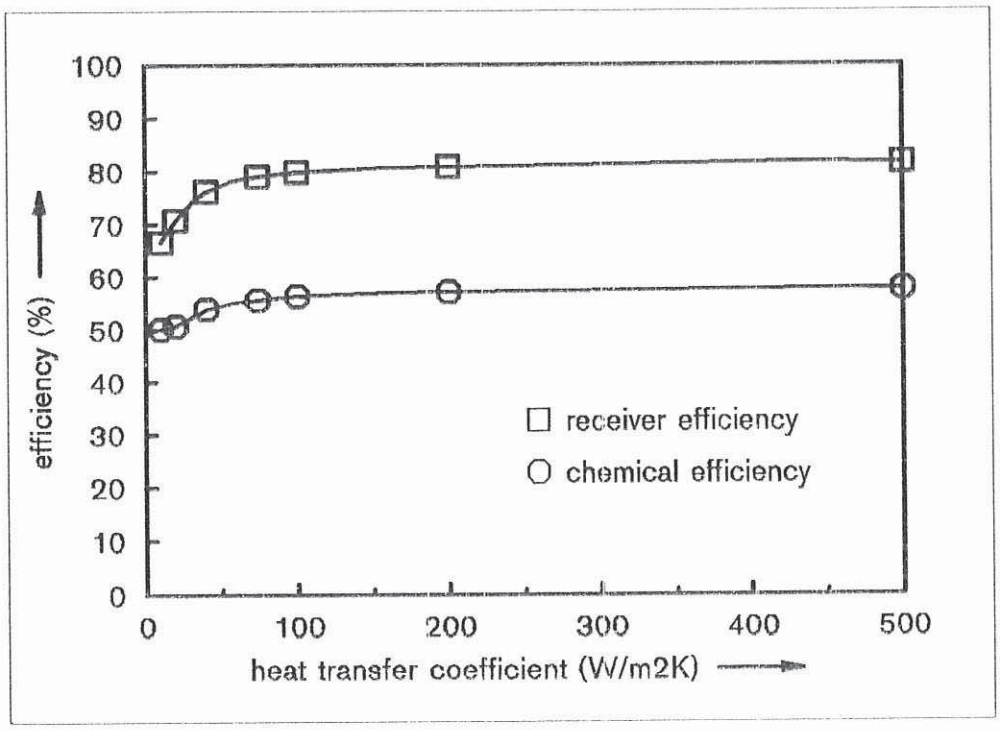


**Figure 21. Influence of Convective Heat Transfer Coefficient on Efficiencies**

Since the determination of heat transfer coefficients in porous structures like reticulated foams is not very well developed, there is a great uncertainty in the used data. Therefore, it

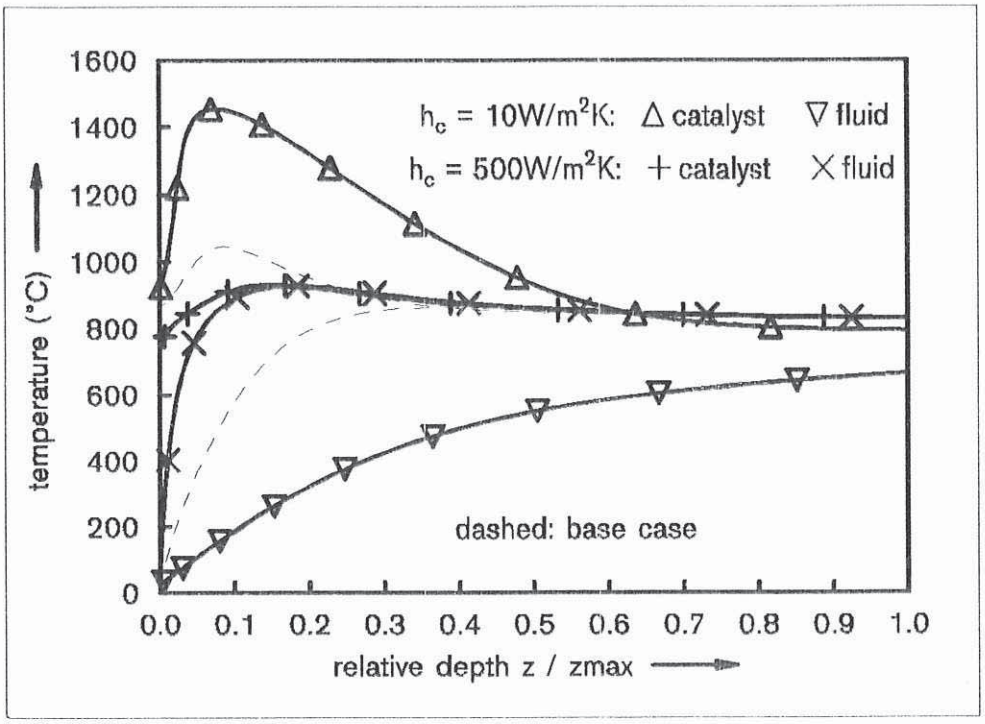


**Figure 22. Temperature Profiles for various Convective Heat Transfer Coefficients** (temperature profiles of base case for comparison)

is necessary to know the impact of varying the heat transfer coefficient on the obtained results. The range of variation for this coefficient was chosen from 10 to 500W/m²K. The base case heat transfer coefficient is 74W/m²K. The influence of a varied heat transfer coefficient is shown in Figure 21 on page 35 with constant methane conversion of 95%. At heat transfer coefficients above 100W/m²K there is very little influence, below that value the efficiencies start to decrease. Especially the receiver efficiency shows a strong dependance at low heat transfer coefficients. The reason for this is twofold and is shown in Figure 22. On one hand the absorber temperatures in the front region increase dramatically thus increasing thermal reradiation losses. On the other hand the fluid is far from thermal equilibrium at the absorber exit, indicated by the temperature difference between catalyst and fluid. Therefore, the amount of sensible energy absorbed by the fluid is reduced which also lowers the receiver efficiency.

The impact on chemical efficiency is less pronounced. Since chemical conversion is based on the catalyst temperature, the higher absorber temperatures (resulting from lower heat transfer coefficients) make the chemical conversion more effective. Since exit methane conversion was kept constant at 95% a lower receiver efficiency means also a lowered fluid mass flow. This is reflected by the moderate decrease in chemical efficiency.

The value of the convective heat transfer for the base case was determined for the CAESAR absorber from single-wire correlations. Some comments should be made here:

- the chosen heat transfer coefficient was derived for a lower mass flow rate per area. Higher flow rates increase the convective heat transfer meaning that the coefficients used are believed to be conservative estimates.

- new absorbers will have higher porosities and therefore thinner elements (struts). This also results in an improved convective heat transfer.

From these points it could be concluded that the convective heat transfer is not a critical aspect in receiver design. Nevertheless more research work is necessary to determine appropriate correlations to calculate the convective heat transfer.

### 5.2.8 Absorber with Multiple Layers

The reason to build the absorber from multiple layers is twofold:

1. the radiative energy absorbed per length unit could be varied
2. the required absorber thickness could be reduced

The absolute amount of absorbed radiation per depth unit depends on the absorption coefficient and the local intensity of solar radiation. Since the intensity of solar radiation is an exponential function of depth the amount of absorbed radiation decreases with increasing depth. If the absorber is then built from multiple layers (beginning with a low PPI-number, i.e. big pores, at the irradiated side followed by layers with smaller pores) the absorption per depth unit could be raised relatively from each layer to the next.

The second reason is more of interest in terms of the construction of a receiver. Using bigger pores in the front of the absorber and smaller in the back results (for the same optical depth) in a thinner absorber (see also 5.2.4.2 on page 30 for comparison). This could be advantageous for future (complex) receiver geometries.

Two different cases are considered in comparison to the base case configuration. Common to both cases is the first layer of the absorber. This layer is built of PPI 5 material and has a thickness of 5mm. Catalyst loading and radiative properties are equal to the base case. This means that under the given irradiation conditions about 16.2% of the collimated radiation is passing this layer without interaction, the rest is either absorbed or scattered. The second layer is built from PPI 20 material. The thickness of this layer is designed for an optical depth of 16.39 for the whole absorber, as with the base case design. The catalyst loading of the second layer was chosen to give a total catalyst mass of 0.02545kg, and the convective heat transfer coefficient is assumed to be 74W/m²K. The two considered cases are:

case **A**: the radiative properties are taken as measured on the CAESAR test samples, together with the corresponding numbers for convective heat transfer area and coefficient (see Table 2 on page 9)

case **B**: the radiative properties and convective heat transfer area are based on theoretical estimations relative to the base case material (see 5.2.4.2). The solar and infrared albedo are 0.272 and 0.54, respectively.

The important properties for the two cases are listed in Table 13.

| case | $k_t$ solar (1/m) | $k_t$ infrared (1/m) | $A_{cV}$ (m²) | catalyst loading (% weight) | absorber depth (cm) |
|---|---|---|---|---|---|
| A | 955 | 1152 | 1400 | 1.165 | 1.545 |
| B | 1311 | 1439 | 2400 | 1.6 | 1.125 |

**Table 13. Properties and Thickness of Second Layer**

The results of the simulation runs are listed in Table 14 on page 38 together with the base case results. There is very little influence on the efficiencies. Especially with the theoretically estimated properties there is no difference to the base case. In terms of efficiencies the results

give no indication of advantages with a multiple layer design. The main difference is in the thickness of the absorber. With the same energetic performance the thickness of the whole absorber could be significantly reduced compared to an absorber with a single layer of PPI 5 material. But, as stated in 5.2.4.2 a similar reduction in thickness could be achieved by using a single layer of a material with smaller pores.

| case | $\eta_{rec}$ (%) | $\eta_{ch}$ (%) | absorber thickness |
|---|---|---|---|
| base | 79.1 | 55.7 | 50mm |
| A | 78.8 | 55.5 | 20.45mm |
| B | 79.1 | 55.7 | 16.25mm |

**Table 14. Results for Two-Layer Absorbers**

As experienced with the first insert of the CAESAR absorber, the joint between two different layers is critical in terms of material problems. This insert failed because two layers separated. It might therefore be concluded that the use of multiple layer absorber does not seem to be advantageous.

### 5.2.9 Feed Gas Composition

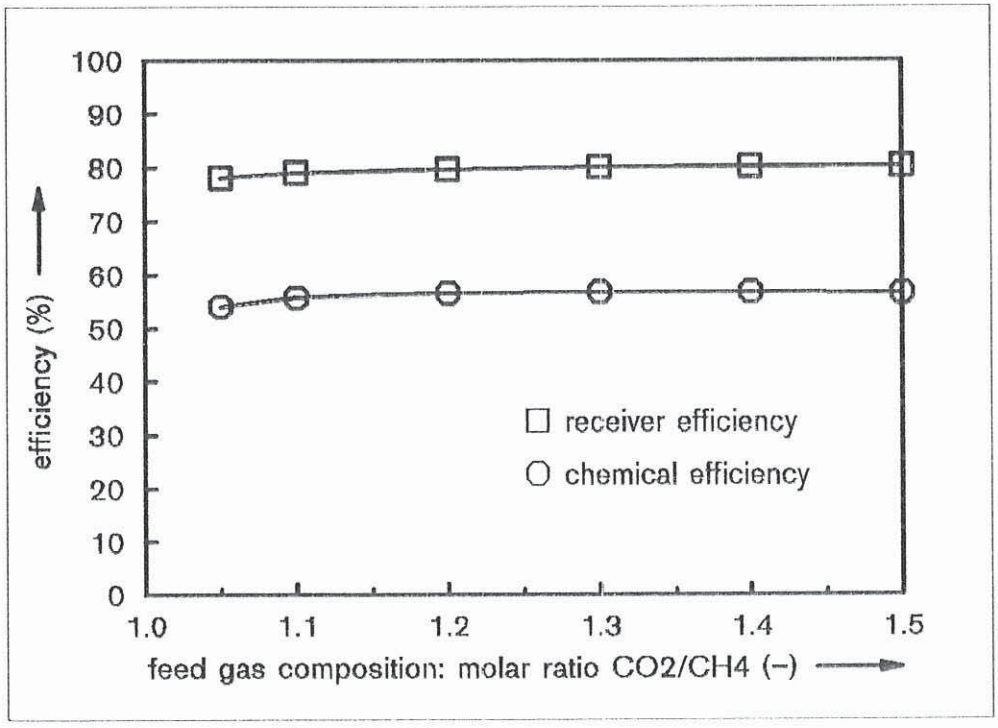


**Figure 23. Influence of Feed Gas Composition on Efficiencies**

The choice of the atomic ratio C:H:O has a strong influence on the chemical reaction. This ratio could be varied by changing the molar composition of the feed gas. The selected range of variation is: $1.05 \leq CO_2/CH_4 \leq 1.5$. In all cases the exit methane conversion was kept constant at 95% by adapting the mass flow.

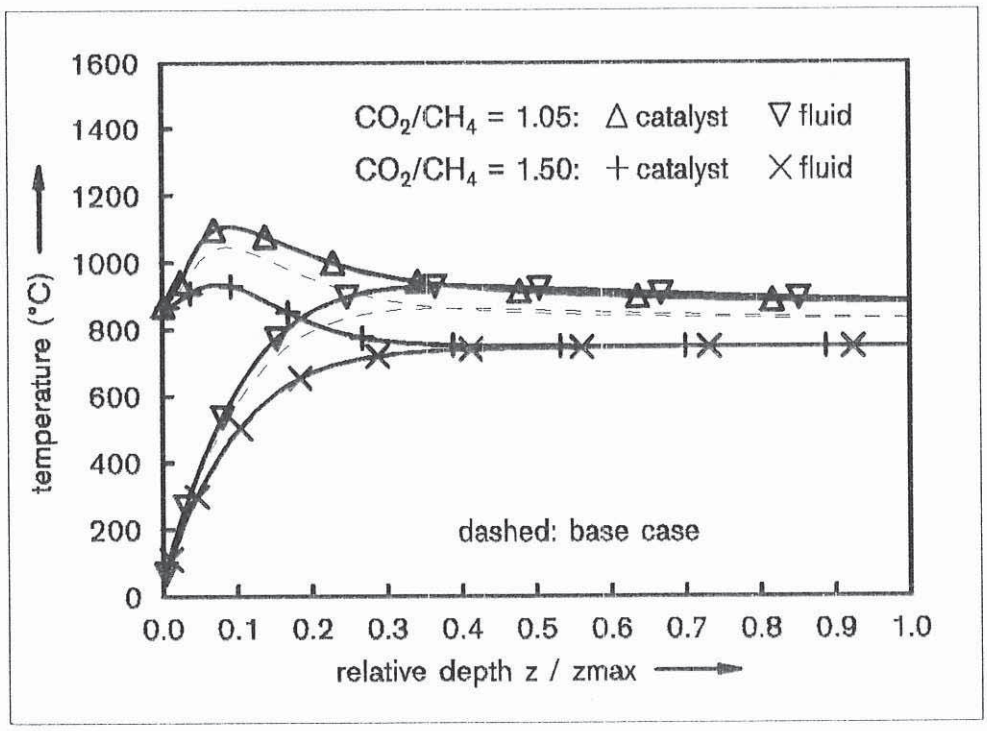


**Figure 24. Temperature Profiles for various Feed Gas Compositions** (temperature profiles of base case for comparison)

The resulting efficiencies are shown in Figure 23. The influence of varied feed gas composition is not very pronounced. At small $CO_2/CH_4$-ratios exists a slight decrease especially in chemical efficiency. At a ratio of 1.05 the chemical efficiency reaches 54.1%, whereas the maximum value is 56.8% (at a molar ratio of 1.3). The receiver efficiency increases slightly from 78.1% (at molar ratio of 1.05) to 80.3% (at a molar ratio of 1.5).

The increase in receiver efficiency could be explained by a lowered absorber temperature level, as shown in Figure 24. Two different effects could be identified to cause this behaviour:

1. the equilibrium temperature for the 95% methane conversion increases with decreasing molar ratio. This means that the temperature level especially in the back part of the absorber is increased too.

2. the reaction kinetics inside the absorber are different. At small $CO_2/CH_4$-ratios the amount of newly formed CO and $H_2$ increases more rapidly throughout the absorber than at higher ratios. By driving the reverse reaction the chemical reaction rates are reduced and the catalyst temperature raises. This effect could be observed in the front region of the absorber.

Both effects can be found in Table 15 where the equilibrium temperature $T_{eq}$ and the fluid exit temperature $T_{fl,ex}$ are given. The table includes also the power figures for sensible heat ($P_{sens}$), methane reforming reaction ($P_{R1}$) and the watergas shift reaction ($P_{R2}$). From the latter it could be easily recognized that with increasing $CO_2/CH_4$-ratio the power absorbed by this reaction is rising, that means the water forming reaction is more promoted. This results in an increased water content in the exit gas which might cause problems (e.g. need of additional condenser facilities). With $CO_2/CH_4 = 1.5$ the water content reaches 4.7% whereas the

| ratio $CO_2/CH_4$ | $T_{fl,ex}$ (K) | $T_{eq}$ (K) | $P_{sens}$ (kW) | $P_{R1}$ (kW) | $P_{R2}$ (kW) | $\dot{m}$ ($10^{-3}kg/s$) |
|---|---|---|---|---|---|---|
| 1.05 | 885.0 | 825.1 | 67.9 | 151.1 | 1.8 | 39.97 |
| 1.10 | 832.2 | 807.2 | 66.3 | 155.2 | 2.5 | 42.50 |
| 1.20 | 791.3 | 784.6 | 65.7 | 156.7 | 3.5 | 45.78 |
| 1.30 | 771.4 | 769.4 | 66.0 | 156.4 | 4.3 | 48.68 |
| 1.40 | 757.9 | 757.9 | 66.7 | 155.6 | 4.9 | 51.33 |
| 1.50 | 747.5 | 748.4 | 67.3 | 154.3 | 5.6 | 53.81 |

**Table 15. Operation Characteristics for Various Feed Gas Compositions**

content in the base case is 2.3%. This is important when the mixture is cooled down for transportation and storage, and the water has to be condensed.

The corresponding mass flow numbers are also included in this section. Relative to the base case the mass flow is increased by about 27% when the feed gas ratio is set to 1.5. This requires more pumping power and/or larger diameter of the connection tubing both resulting in higher costs. A ratio of 1.1 to 1.2 seems a good compromise between all the mentioned aspects.

### 5.2.10 Operation with Partial Conversion

To operate a volumetric receiver-reactor in a solar tower raises the question how a receiver would look like which covers the complete focal spot. One approach is to build the receiver by a large number of sub-receivers (called modules), each with a (hexagonal) secondary in front. However this implies that the sub-units located at the outer side of the focal spot experience relatively low solar flux densities compared to those modules located near the center.

It might therefore be advantageous to operate those units located in zones with lower flux density as prereactors. This implies a serial connection of several modules with the first stage operating for example from a conversion level of 10% (inlet composition) to 40% (exit composition). The next stage could then perform the reaction until the desired conversion level (e.g. 95%).

To determine the behaviour of such a serial assembly the first stage and the final stage were examined. For the first stage it was assumed that the feed gas enters with a conversion level of 10% (due to incomplete reverse reaction in the methanator of a closed loop system) and with the corresponding equilibrium temperature (465°C). The resulting efficiencies, obtained by varying the feed gas flow, are shown in Figure 25. It is obvious that the efficiencies remain nearly constant although the exit methane conversion of this first stage is varied from 30% to 60%.

The outer units of a modular receiver array for a solar tower will experience relatively low irradiation levels. To evaluate the receiver performance when these outer units are operated as first stage of the serial assembly, calculations with lower flux densities and low conversion levels were performed. The results confirmed that this operation mode might be advantageous. For a solar flux density of 100kW/m² and an exit conversion of 50% the receiver and chemical efficiency is 70.1% and 59.9%, respectively. The corresponding numbers for the same inlet conditions (feed gas with 10% methane conversion at equilibrium temperature) but an exit methane conversion of 95% are 61.2% for the receiver efficiency and 50.8% for the chemical efficiency. This is a relative increase in chemical efficiency of about 20%.

The results for the final stage look quite different. Operating a module with higher feed gas conversion levels (and the corresponding equilibrium temperature as inlet temperature) leads to a drastic drop in efficiencies. For a inlet conversion of 50% the receiver efficiency is

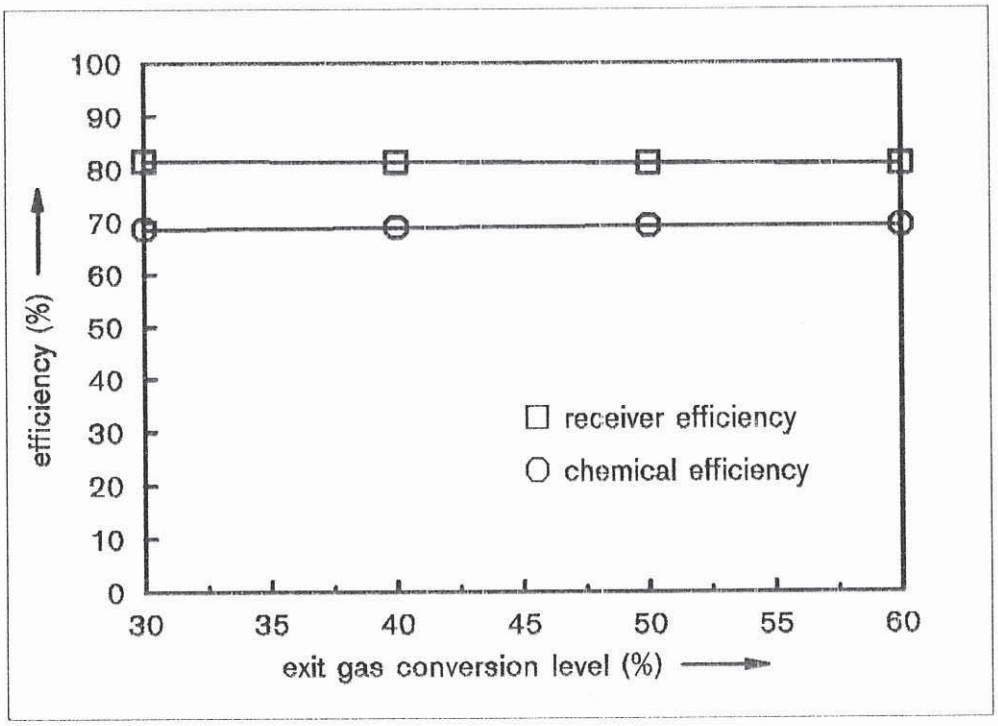


**Figure 25. Influence of Exit Conversion on Efficiencies (First Stage)** (feed gas methane conversion of 10%)

61.5%, whereas the chemical efficiency reaches 39.9%. The reason for this behaviour is a significant increase in absorber temperatures, as shown in Figure 27 for the base case catalyst loading of 0.4%. Once again the changed chemical composition (lower partial pressure of $CO_2$ and $CH_4$ in the fluid) lowers the reaction rates, thus leading to higher catalyst temperatures to perform the desired conversion.

One way to overcome this disadvantage is to enhance the catalyst performance, e.g. by increasing the catalyst loading. For a catalyst loading of 2.0% the corresponding temperature profiles are included in Figure 27 on page 40. The receiver efficiency for this case is calculated to be 77.9% and the chemical efficiency to be 62.0%. To compare these figures with the base case it should be kept in mind that the fluid enters the receiver at equilibrium temperature (618.6°C for the mentioned feed gas conversion). But nevertheless it is clear that the receiver efficiency could be improved by increasing the catalytic activity.

To answer the question whether it makes sense to operate a number of staged modules requires a detailed study based on a realistic solar flux distribution. An additional advantage could be that the connection in series might behave less sensitive to solar flux variations. But this effect should also be examined more in detail in a realistic array of modules.

### 5.2.11 Receiver Pressure

Operation of volumetric receiver-reactors in a closed loop or another chemical process might require increased system pressure. The pressure has a significant impact on the equilibrium composition of the fluid mixture. This means that for a given methane conversion a higher temperature is needed when the pressure is increased. The pressure is varied from 0.5bar to

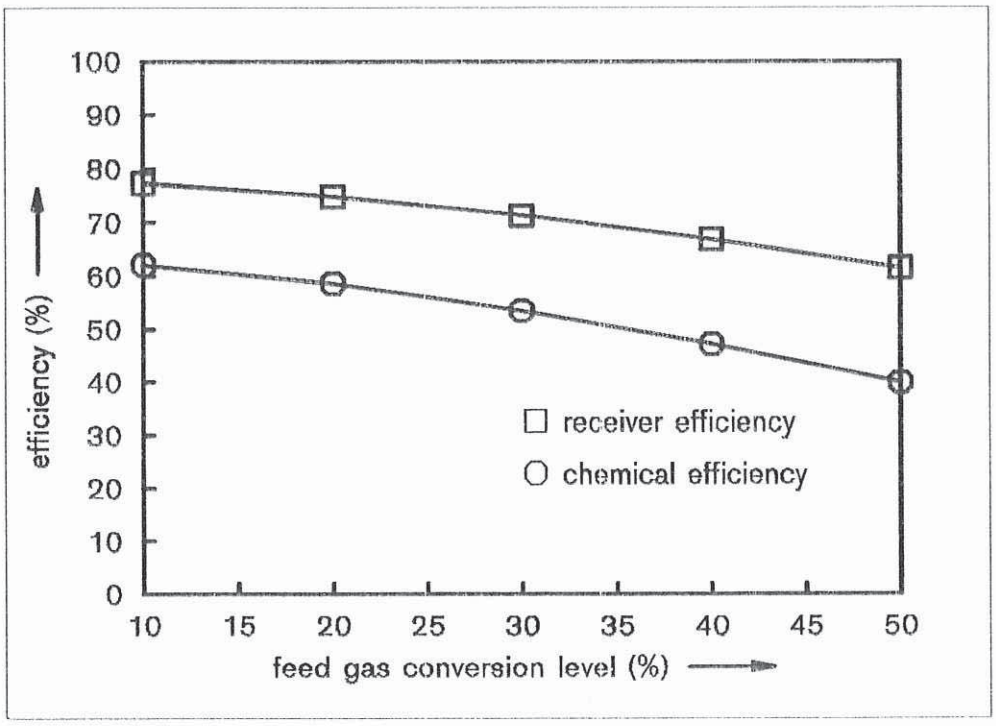


**Figure 26. Influence of Extent of Prereaction on Efficiencies (Final Stage)** (exit methane conversion of 95%)

10bar, while the base case pressure is 1bar. The results of this variation are given in Figure 28 on page 44.
On the first view the results look quite surprising. Lower system pressure means for a given methane conversion (here 95%) a decrease in equilibrium temperature. Therefore it was expected that the overall receiver temperature level is also decreased, with the consequence of higher efficiency. But, as shown in the figure, this does not hold at low pressures. Further investigation of the reason for this behaviour reveals that the reaction rates (especially inside the absorber after a certain amount of reaction) are smaller at low pressures. This results in higher temperatures necessary to drive the reaction to the desired conversion level (see Figure 29). The higher radiative losses lower then the efficiencies. This effect becomes very pronounced at system pressures below 1bar.

Generally the receiver efficiency remains nearly constant at pressure levels above 1bar. With increasing pressure the equilibrium temperature for the 95% methane conversion is raised. Thus the fluid exit temperature which is normally slightly above equilibrium temperature (due to finite reaction kinetics) is raised too. This means that the amount of sensible heat increases in the same way which is expressed by the decreasing chemical efficiency at higher pressures.

Figure 29 gives good insight into the influence of reaction kinetics. Especially in the front region of the absorber the profiles of the catalyst temperature are quite different. The profile for a pressure of 2bar starts at lower values and has a low slope at the front end. The temperature rise start more inside the absorber than in the lower pressure cases where the slope at the front end is significantly steeper. Since the absorber temperatures in the front section are mainly responsible for the thermal radiation losses the higher temperature level explains the sharp drop in efficiency.

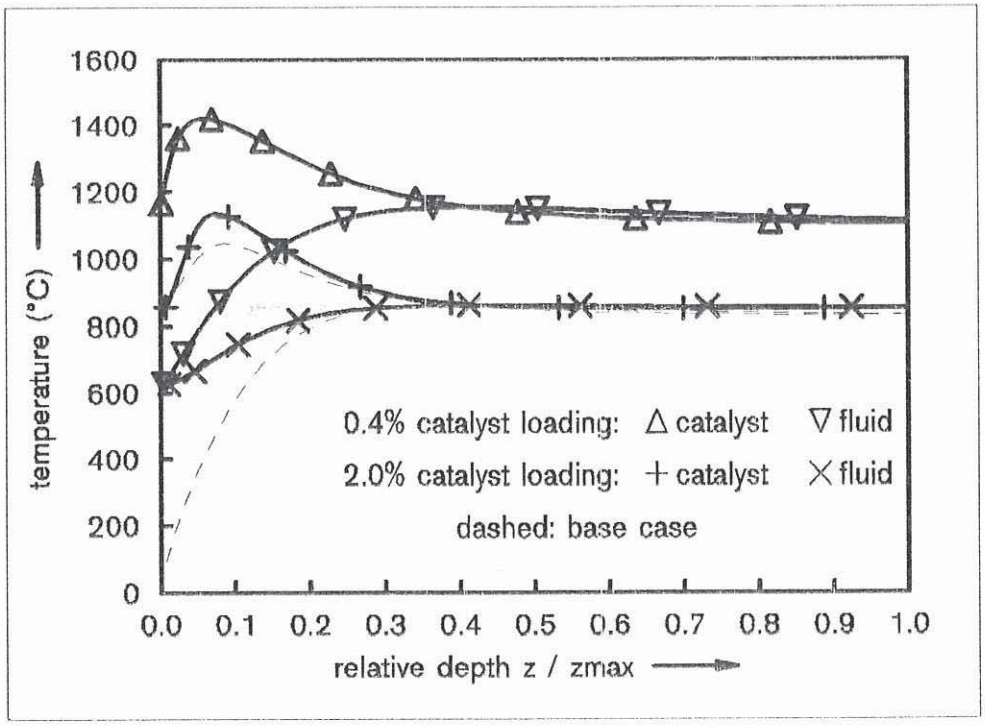


**Figure 27. Temperature Profiles for operation from 50 to 95% conversion** (temperature profiles of base case for comparison)

Interpreting the data raises the question whether the chemical rate equations, which were determined at a pressure of 1atm, are applicable to other pressures without modification, or if this leads to erratic results. Further research is necessary to answer this question.

### 5.2.12 Sensible Heat Exchange

To make use of the sensible heat in the exiting gas mixture the easiest possibility is the addition of a counterflow heat exchanger to preheat the fluid entering the receiver. To investigate the influence of this measure the heat exchanger efficiency was varied in the range from 0.0 to 90%. For simplicity reasons it was assumed that the heat capacity of the fluid is independent of temperature and composition. Using this simplification the heat exchanger efficiency could be defined by temperature ratios as follows:

$$\eta_{hx} = \frac{T_{i,2} - T_{i,1}}{T_{e,1} - T_{amb}} \tag{34}$$

For the calculations it was further assumed that the feed gas is available at ambient temperature ($T_{i,1} = T_{amb}$). A schematic of the system with the corresponding temperatures is given in Figure 30.

As shown in Figure 31, the receiver efficiency remains nearly constant. But the chemical efficiency is increasing almost linearly with heat exchanger efficiency. This is expected since the amount of energy which is otherwise needed for sensible gas heating is now used in the reaction of additional gas. This is also expressed by the fact that the mass flow necessary to obtain 95% conversion in the exit increases with improved heat exchange (not shown here).

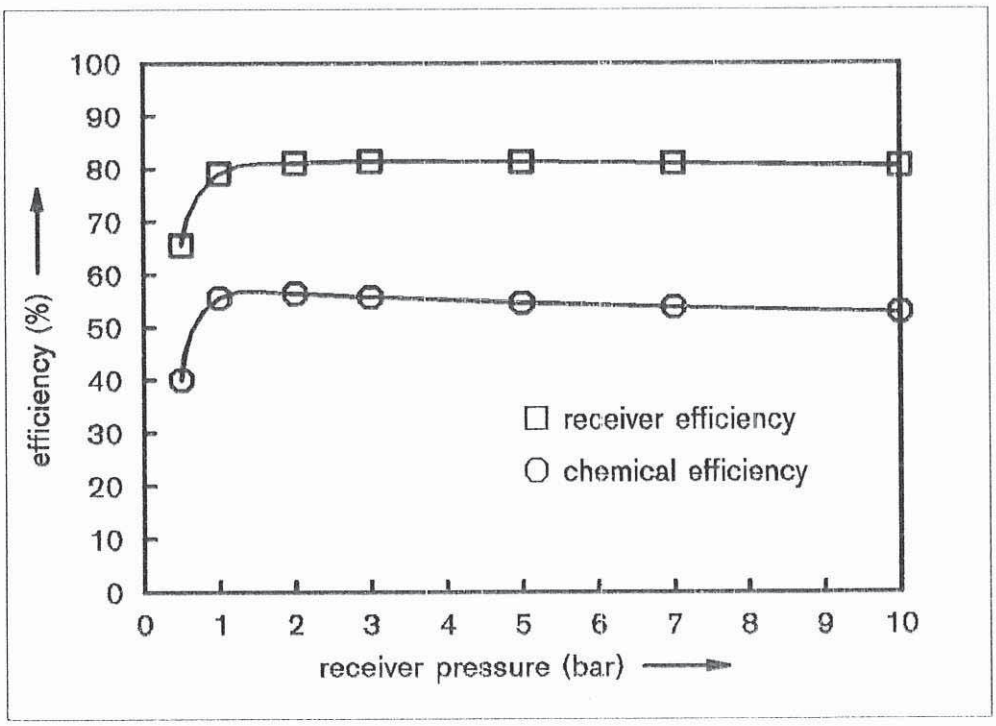


**Figure 28. Influence of Receiver Pressure on Efficiencies**

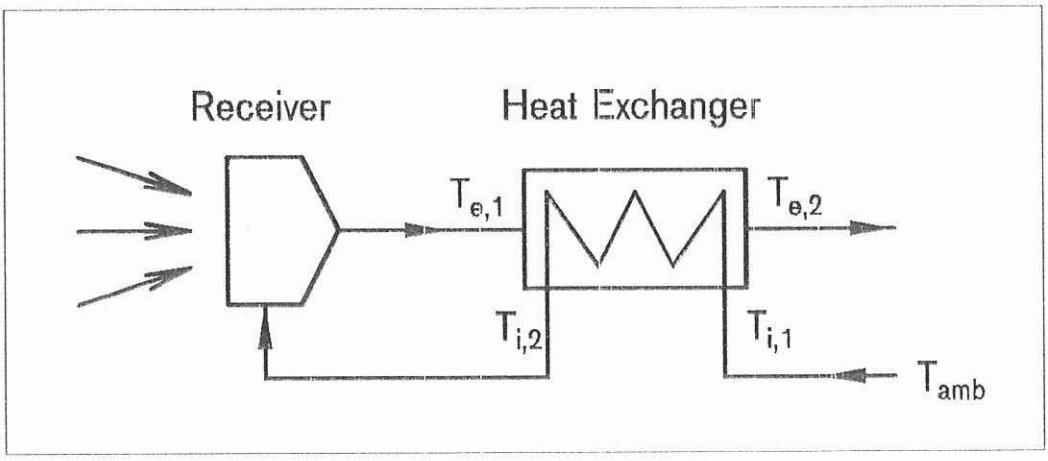


**Figure 30. Schematic of the Receiver with Heat Exchanger**

On the other hand, the receiver losses remain nearly uninfluenced from the heat exchange. This behaviour could be understood by the temperature profiles in Figure 32. The overall change of the catalyst temperatures is not very pronounced. Therefore, the losses (determining the receiver efficiency) don't vary either that much. Here once again it is obvious that the convective heat transfer is a secondary energy transfer mechanism. Although with a very efficient heat transfer the temperature difference between fluid and catalyst in the front

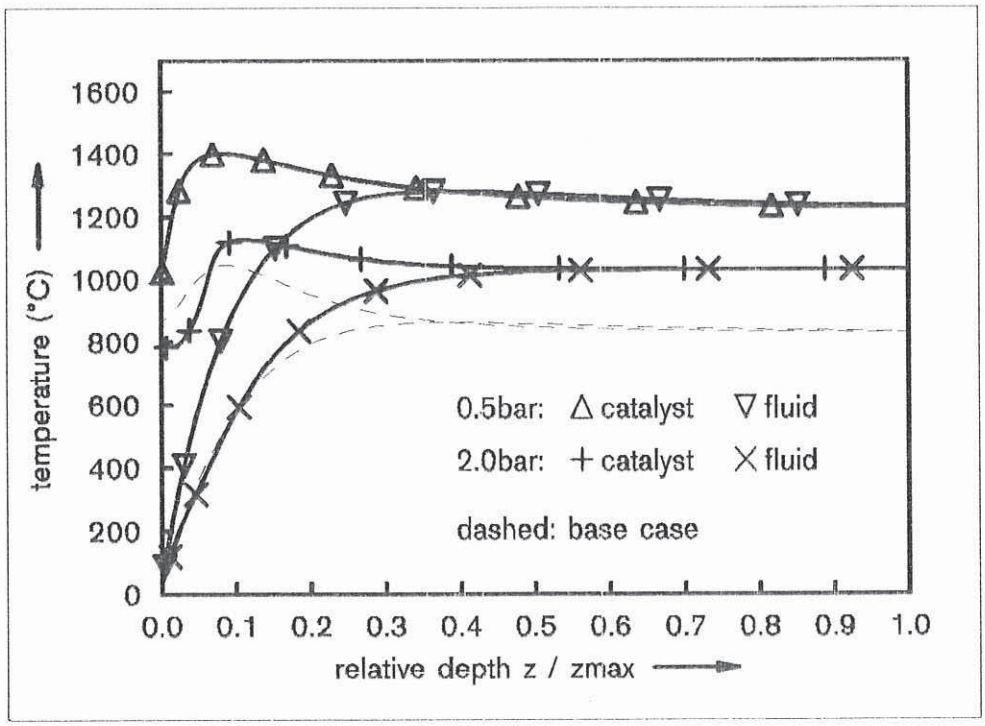


**Figure 29. Temperature Profiles for Various Receiver Pressures** (temperature profiles of base case for comparison)

region is pretty small compared to the base case this shows very little influence on the catalyst temperature in that region.

As the purpose of receiver-reactors generally is a high chemical efficiency the use of counterflow heat exchangers is one of the most important improvements in system design. This heat exchanger could be either a conventional heat exchanger, or it could be used as a prereactor on the inlet side. This could be done by giving the inlet gas stream the possibility to react towards its equilibrium composition after exceeding a certain temperature limit. For instance if the temperature of the inlet stream is above 500°C the chemical equilibrium temperature is (dependent on system pressure) generally below this value. Therefore the presence of catalyst leads to an endothermal reaction while cooling down the fluid. This increases the temperature difference over the heat exchanger elements and therefore either improves the heat exchanger efficiency or allows the use of smaller units. Two possibilities are mentioned how to build such a 'reactive' heat exchanger in practice:

1. by dividing the complete heat exchanger in several sub-units where in the high-temperature sections a conventional adiabatic reactor is connected in the inlet stream inbetween two subsequent sections
2. by constructing the high-temperature sections of the inlet stream as conventional heated reactor (e.g. by filling the tubes with catalyst pellets or depositing catalyst on the walls of the tubes)

The latter possibility should be most effective since the tube walls have the highest temperature. Further studies should verify if these 'reactive' heat exchangers are feasible and economic.

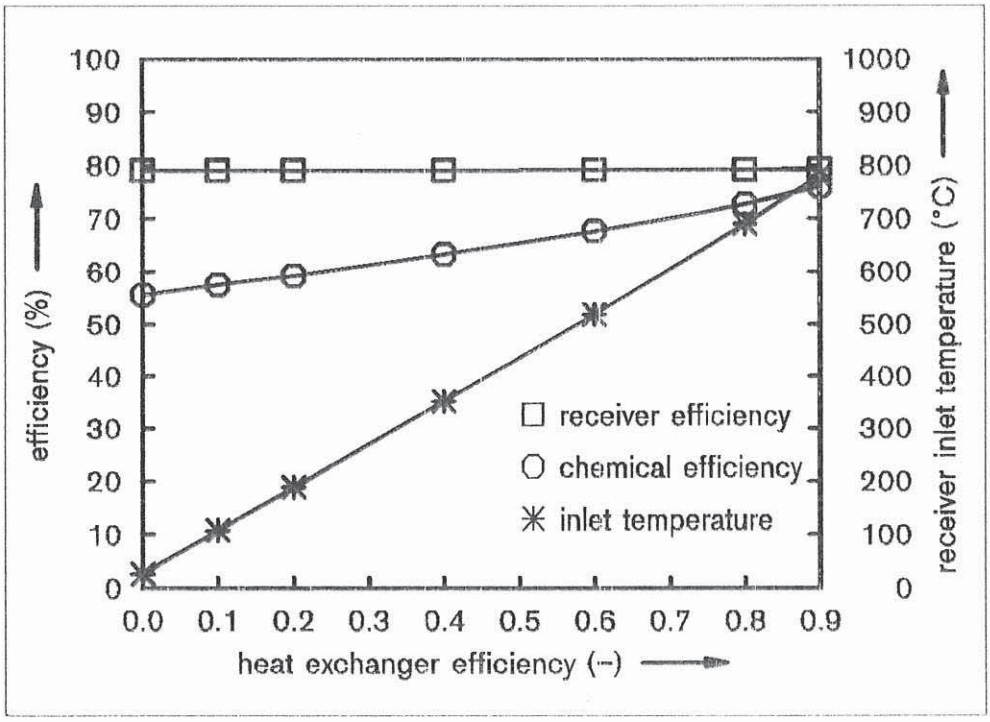


**Figure 31. Influence of Heat Exchange on Efficiencies**

### 5.2.13 Optimization of Receiver Geometry

Another very important improvement is the adaption of the receiver geometry. This adaption covers various aspects:

- shaping of the window to reduce solar reflection losses (e.g. by a paraboloidal window geometry)
- increasing of absorber surface with respect to aperture area reduces the solar flux density
- dividing the absorber into two different zones: a zone where radiation and fluid flow are in parallel (main absorber regime) and another zone with radiation and fluid flow in opposite direction (fluid entry zone)
- shaping the (main) absorber to homogenize the flux density on the surface (iso-flux absorber)
- tailoring of local fluid flow to local flux density (i.e. by using various pore sizes and absorber thickness)

Some of the upper aspects approximate the concept of a cavity-type receiver with the known advantages in terms of efficiency and flux distribution. A schematic of how such a receiver would look like is given in Figure 33. The proper layout of all mentioned parameters is very critical and strongly dependent on the concentrating system defining the solar flux distribution. The tools to design a receiver for a given concentrator are under development at DLR Stuttgart and will be subject of following reports.

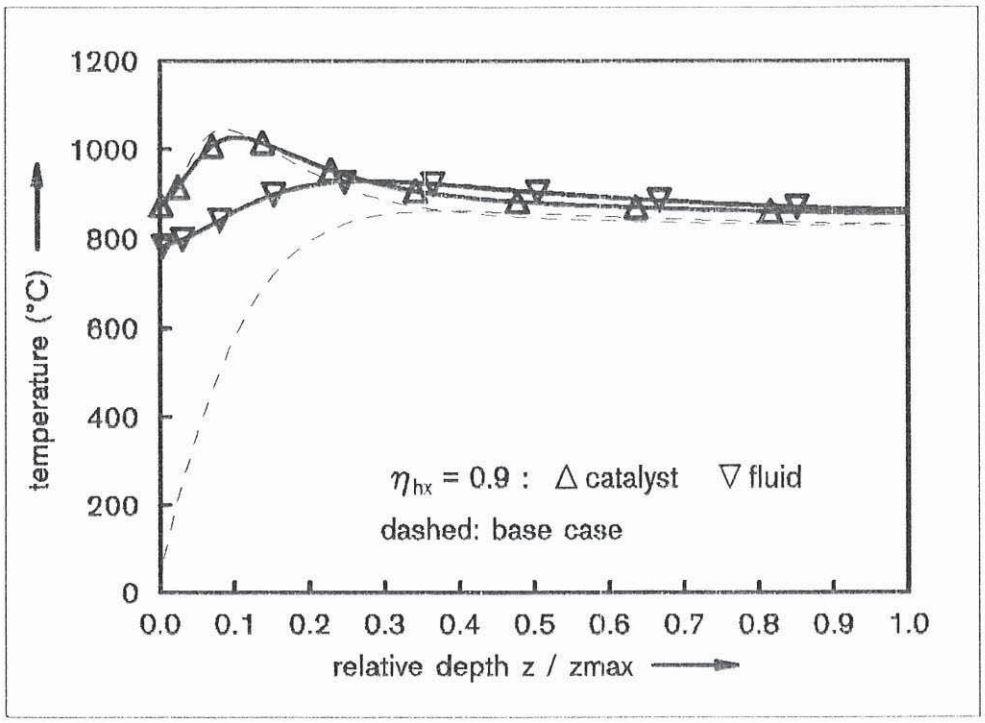


**Figure 32. Temperature Profiles for Heat Exchanger Efficiency of 0.9** (temperature profiles of base case for comparison)

### 5.3 Conclusions

Since the energy transport mechanisms in a volumetric receiver-reactor depend on a big number of different factors the results of the parameter study might be confusing. As stated before, the simulations are based on a simplified receiver model. Therefore, the results should be taken as indicators of trends. But nevertheless, some important conclusions could be drawn:

- the system is quite sensitive to the proper ratio of mass flow and incident power, especially when high methane conversion is desired. Therefore, proper system control is essential to prevent undesirable high absorber temperatures which result in reduced efficiencies and increase the risk of absorber damage.
- the receiver could be operated with good performance even at relatively low solar flux levels.
- a high catalytic activity is important since this is the main energy transfer mechanism. Depending on local radiation intensity there exists a minimum activity to achieve good performance whereas a further increase in activity doesn't improve the efficiency significantly.
- further research work is necessary about the influence of pore size and porosity of the absorber to provide a reliable data base for the absorber properties. If the theoretically derived correlations hold then there is no advantage in the use of a certain pore size material and only little advantage in the use of high porosity structures.
- the albedo of the absorber (defining the backscattered fraction of radiation) should be minimized to reduce losses.

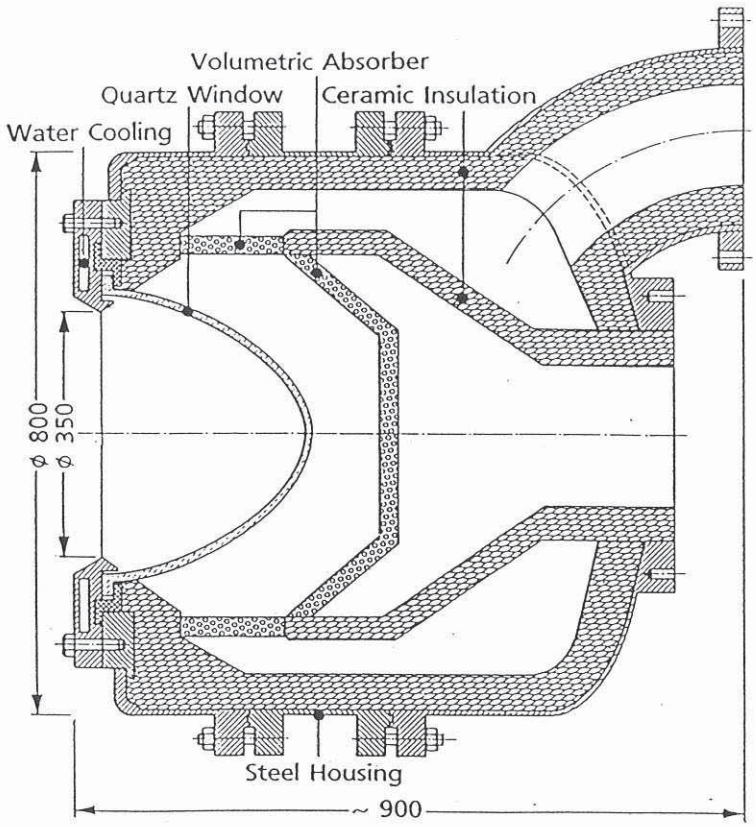


**Figure 33. Example of an Optimized Receiver Layout**

- convective heat transfer is a second order effect. Nevertheless more research work is necessary to improve the calculation of convective heat transfer coefficients.
- the use of multiple layers doesn't improve performance but suffers from the risk of separation at the layer joints.
- a feed gas ratio $CO_2/CH_4$ of 1.1 to 1.2 looks most promising.
- operation of a multiple receiver system (with partial conversion in each) is dominated by the performance of the final stage. If reactors could be built with superior catalytic characteristics this might be a good possibility to build large receiver arrays for tower plants.
- the receiver pressure is critical at very low pressures, due to reduced chemical reaction rates. Higher pressure has little effect on receiver efficiency but chemical efficiency is decreasing slightly.
- the addition of a counterflow heat exchanger is the key aspect to improve the chemical efficiency.

These general conclusions can help in understanding the characteristics of a volumetric receiver-reactor. For the design of a certain receiver it is indispensible to perform the simulation under the specific operation conditions. The optimum performance (in thermodynamic, chemical or economical sense) differs from one application to another.

## 6. Summary

A theoretical model developed at DLR Stuttgart was used to simulate the performance of volumetric receiver-reactors. In order to verify the validity of the simulation results the predicted performance was compared to the measured data obtained during the CAESAR experiments. The overall receiver performance (receiver and chemical efficiency, methane conversion) was predicted quite well, generally with a slight overestimation (eventually due to the averaging over the receiver zones, thus neglecting the influence of local inhomogeneities in the solar flux and mass flow distribution).

The comparison of axial absorber temperatures showed acceptable agreement between measurements and predictions. This agreement was improved by assuming local mass flow reduction in the zones with peak insolation. This local mass flow reduction is expected from theoretical considerations. However, great uncertainties remain concerning the amount of this reduction. The agreement between measurements and predictions is also affected by the uncertainties in catalytic activity (which might change with location and test time due to deactivation and sintering effects) and other parameters (solar flux distribution, radiative properties etc.). Nevertheless the obtained results indicated that the model is capable to predict overall performance and local trends satisfactorily.

In the second part the model was used for a parameter study to identify sensitive parameters and to evaluate the potential of the concept of a volumetric receiver-reactor. The varied parameters included: solar flux density, methane conversion, catalyst activity, structural and radiative properties of the absorber, convective heat transfer coefficient, inlet gas composition and receiver pressure. The influence of sensible heat exchange and other system aspects on the performance of a complete plant were also evaluated.

The study showed that the key aspects for a good receiver performance are: the chemical activity of the catalyst (chemical reaction is the major energy transfer mechanism); optical properties to ensure effective absorption of solar radiation; proper system control for the mass flow in relation to insolation and operation conditions. Concerning the system performance the addition of a counterflow heat exchanger to preheat the entering fluid mixture is of major importance. With an efficient recuperator the amount of energy stored in the chemical reactions could be significantly increased.

From the results it could be concluded that volumetric receiver-reactors have a high potential for the application to direct chemical reactions driven by solar radiation. However, further work is necessary on the simulation model and on the evaluation of basic absorber properties. Improvements of the model should include the local fluid pressure drop to account for the influence of local mass flow variations. More experimental work is required to improve the knowlegde about catalyst aspects and properties of porous materials like ceramic foams. On the other hand some technical problems must be solved too before these systems could be applied.

## 7. Bibliography


[1] Hogan,R.E.; Skocypec,R.D.: *Analysis of Catalytically Enhanced Solar Absorption Chemical Reactors: Part I - Numerical Model Description; Part II - Predicted Characteristics of a 100kW (chemical) Reactor* SED - Vol.8, Solar Energy Technology, 1989

[2] Buck,R.: *Modellierung volumetrischer Receiver* DLR Stuttgart, Interner Bericht DLR IB 90105, 1990 (in German)

[3] Siegel,R.;, Howell,J.R.: *Thermal Radiation Heat Transfer* Hemisphere Publishing Corporation, New York (1981)

[4] Richardson,J.T.; University of Houston,Texas, USA *private communication* data presented at IEA-SSPS Task V-meeting, 2.-3.february 1989 SNLA, Albuquerque, NM

[5] J.F.Muir, R.E.Hogan, R.D.Skocypec and R.Buck: *The CAESAR Project: Experimental and Modeling Investigation of Methane reforming in a CAtalytically Enhanced Solar Absorption Receiver on a Parabolic Dish* Sandia Report SAND90-2987, Sandia National Laboratories, Albuquerque, NM (to be published)

[6] R.Buck, J.F.Muir, R.E.Hogan and R.D.Skocypec: *Carbon Dioxide Reforming of Methane in a Solar Volumetric Receiver-Reactor: The CAESAR Project* Proceedings of the 5th Symposium on Solar High Temperature Technologies, August 27-31, 1990, Davos, Switzerland (to be published)

[7] J.F.Muir, R.E.Hogan, R.D.Skocypec and R.Buck: *Solar Reforming of Methane in a Direct Absorption Catalytic Reactor on a Parabolic Dish: I - Test and Analysis* 1991 ASME-JSME International Solar Energy Conference, Reno, Nevada, March 17-22, 1991

[8] R.D.Skocypec, R.E.Hogan and J.F.Muir: *Solar Reforming of Methane in a Direct Absorption Catalytic Reactor on a Parabolic Dish: II - Modeling and Analysis* 1991 ASME-JSME International Solar Energy Conference, Reno, Nevada, March 17-22, 1991

[9] Kleih,J.: *Beurteilung von konzentrierenden Spiegelsystemen mit Hilfe des Meßsystems HERMES und des Simulationsprogrammes HELIOS* DLR-Report FB 89-51, 1989 (in German)

## A.1 CAESAR: Receiver Zone Description Table

| zone number | area ($m^2$) | position | description |
|---|---|---|---|
| 1 | $7.0686 \cdot 10^{-2}$ | central disk | volumetric absorber |
| 2 | $2.6507 \cdot 10^{-2}$ | outer ring, $\theta = 0°$ | volumetric absorber |
| 3 | $2.6507 \cdot 10^{-2}$ | outer ring, $\theta = 45°$ | volumetric absorber |
| 4 | $2.6507 \cdot 10^{-2}$ | outer ring, $\theta = 90°$ | volumetric absorber |
| 5 | $2.6507 \cdot 10^{-2}$ | outer ring, $\theta = 135°$ | volumetric absorber |
| 6 | $2.6507 \cdot 10^{-2}$ | outer ring, $\theta = 180°$ | volumetric absorber |
| 7 | $2.6507 \cdot 10^{-2}$ | outer ring, $\theta = 225°$ | volumetric absorber |
| 8 | $2.6507 \cdot 10^{-2}$ | outer ring, $\theta = 270°$ | volumetric absorber |
| 9 | $2.6507 \cdot 10^{-2}$ | outer ring, $\theta = 315°$ | volumetric absorber |
| 10 | $5.655 \cdot 10^{-2}$ | ring wall | fluid inlet channel |
| 11 | $7.0686 \cdot 10^{-2}$ | central disk | inner surface of quartz window |
| 12 | $2.6507 \cdot 10^{-2}$ | outer ring, $\theta = 0°$ | inner surface of quartz window |
| 13 | $2.6507 \cdot 10^{-2}$ | outer ring, $\theta = 45°$ | inner surface of quartz window |
| 14 | $2.6507 \cdot 10^{-2}$ | outer ring, $\theta = 90°$ | inner surface of quartz window |
| 15 | $2.6507 \cdot 10^{-2}$ | outer ring, $\theta = 135°$ | inner surface of quartz window |
| 16 | $2.6507 \cdot 10^{-2}$ | outer ring, $\theta = 180°$ | inner surface of quartz window |
| 17 | $2.6507 \cdot 10^{-2}$ | outer ring, $\theta = 225°$ | inner surface of quartz window |
| 18 | $2.6507 \cdot 10^{-2}$ | outer ring, $\theta = 270°$ | inner surface of quartz window |
| 19 | $2.6507 \cdot 10^{-2}$ | outer ring, $\theta = 315°$ | inner surface of quartz window |
| 20 | $7.0686 \cdot 10^{-2}$ | central disk | outer surface of quartz window |
| 21 | $2.6507 \cdot 10^{-2}$ | outer ring, $\theta = 0°$ | outer surface of quartz window |
| 22 | $2.6507 \cdot 10^{-2}$ | outer ring, $\theta = 45°$ | outer surface of quartz window |
| 23 | $2.6507 \cdot 10^{-2}$ | outer ring, $\theta = 90°$ | outer surface of quartz window |
| 24 | $2.6507 \cdot 10^{-2}$ | outer ring, $\theta = 135°$ | outer surface of quartz window |
| 25 | $2.6507 \cdot 10^{-2}$ | outer ring, $\theta = 180°$ | outer surface of quartz window |
| 26 | $2.6507 \cdot 10^{-2}$ | outer ring, $\theta = 225°$ | outer surface of quartz window |
| 27 | $2.6507 \cdot 10^{-2}$ | outer ring, $\theta = 270°$ | outer surface of quartz window |
| 28 | $2.6507 \cdot 10^{-2}$ | outer ring, $\theta = 315°$ | outer surface of quartz window |
| 29 | 0.2827 | aperture | (imaginary) aperture |

**Table 16. Zone Description for CAESAR Simulation Runs** (for explanation of the positions see Figure 2 on page 8)

## A.2 Exchange Factor Table for Parameter Study

| | j = 1 | j = 2 | j = 3 | j = 4 | j = 5 |
|---|---|---|---|---|---|
| i = 1 | 0.065520 | 0.101991 | 0.904879 | 0.000000 | 0.814391 |
| i = 2 | 0.509955 | 0.052489 | 0.475605 | 0.000000 | 0.428044 |
| i = 3 | 0.904879 | 0.095121 | 0.000000 | 0.000000 | 0.000000 |
| i = 4 | 0.000000 | 0.000000 | 0.000000 | 0.000000 | 1.000000 |
| i = 5 | 0.814391 | 0.085609 | 0.000000 | 1.000000 | 0.080000 |

**Table 17. Exchange factors $Y_{i,j}$ for $0 \leq \lambda \leq 3\mu m$**

| | j = 1 | j = 2 | j = 3 | j = 4 | j = 5 |
|---|---|---|---|---|---|
| i = 1 | 0.040950 | 0.099415 | 0.904879 | 0.000000 | 0.000000 |
| i = 2 | 0.497074 | 0.051102 | 0.475605 | 0.000000 | 0.000000 |
| i = 3 | 0.904879 | 0.095121 | 0.000000 | 0.000000 | 0.000000 |
| i = 4 | 0.000000 | 0.000000 | 0.000000 | 0.000000 | 1.000000 |
| i = 5 | 0.000000 | 0.000000 | 0.000000 | 1.000000 | 0.050000 |

**Table 18. Exchange factors $Y_{i,j}$ for $3\mu m < \lambda < \infty$**

## A.3 Basic Correlations for Porous Media

The following estimations are not intended to describe the complex interrelations of porous media exactly, but to show how the general dependences are. Therefore the structure of a 3-dimensional foam material is approximated by a cubic volume element crossed by 3 perpendicular rods. This element is empty except for the solid rods. A complete foam-like structure could then be composed by a cluster of such elements. A schematic of an element is shown in Figure 34.

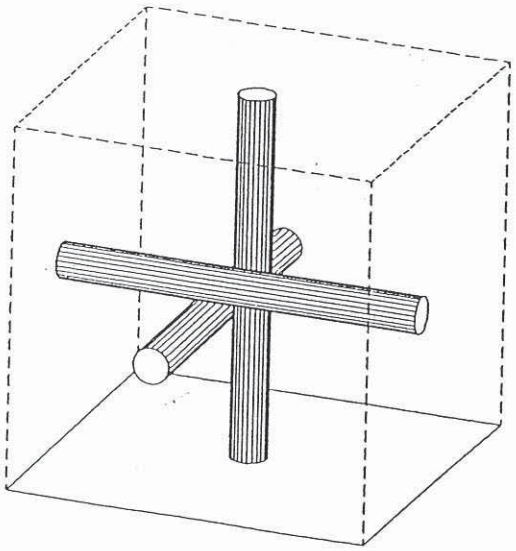

**Figure 34. Schematic of Volume Element for Foam Model** (cube with side length s)

For a simple 'cell' a number of correlations could be derived. The edge dimension of the cube is defined by the length s. Then the volume of the cell is

$$V_{cell} = s^3 \tag{35}$$

The pore size of the structure is then directly proportional to the dimension s. The number generally used to describe foam materials is the PPI-number. This number, given by the number of pores intersected per linear distance of one inch, could then be described by

$$n_{PPI} = \frac{0.0254}{f_{prop} \cdot s} \tag{36}$$

The factor $f_{prop}$ means here a proportionality factor which depends on the cutting direction in the material. Its range is $1 \leq f_{prop} \leq \sqrt{3}$ .

The surface of the rods (corresponding to the struts or webs in the foam material) is given by

$$A_{rod} = 3 \cdot \pi \cdot s \cdot d \tag{37}$$

The total mass of solid contained in the rods is defined by

$$m_{rod} = \frac{3}{4} \cdot \pi \cdot s \cdot d^2 \cdot \rho_{mat} \tag{38}$$

with $\rho_{mat}$ being the material density (i.e. density of alumina).

The bulk density of the structure is given as

$$\rho_{bulk} = \frac{m_{rod}}{V_{cell}} \tag{39}$$

Rewriting this with equations (35) and (38) results in

$$\rho_{bulk} = \frac{3}{4} \cdot \pi \cdot \left(\frac{d}{s}\right)^2 \cdot \rho_{mat} \tag{40}$$

The (macroscopic) porosity $\psi$ is given by

$$\psi = \frac{\rho_{mat} - \rho_{bulk}}{\rho_{mat}} \tag{41}$$

or

$$\psi = 1 - \frac{3}{4} \cdot \pi \cdot \left(\frac{d}{s}\right)^2 \tag{42}$$

The specific surface area per unit volume could be expressed as (using equations (37), (35) on page 4, (36))

$$A_V = \frac{A_{rod}}{V_{cell}} = 3 \cdot \frac{\pi}{s} \cdot \left(\frac{d}{s}\right) \tag{43}$$

This specific surface area is important for convective heat transfer and for catalytic activity. The convective heat transfer is directly proportional to the (macroscopic) surface area. The dependence for the catalytic activity is more complicated. The catalyst is generally deposited on a washcoat of a few microns thickness which is small compared to the dimension of the strut (here approximated by the rods). Assuming that the microstructure of the washcoat, the specific catalyst deposition (catalyst mass per washcoat volume) and the washcoat thickness do not change this means that the catalyst loading (defined as weight percentage of the total mass) is proportional to the available macroscopic surface area of the porous medium. The catalyst loading (% weight) is defined as

$$\Gamma = \frac{m_{cat}}{m_{rod}} \cdot 100 \tag{44}$$

Assuming a constant specific catalyst deposition per (macroscopic) surface area (which is equal to the surface area of the rods) the catalyst loading could be expressed after some rearrangement as

$$\Gamma = \frac{4 \cdot m_{cat,A}}{d \cdot \rho_{mat}} \cdot 100 \tag{45}$$

with $m_{cat,A}$ being the specific catalyst deposition per rod surface area.

The transport of energy by pure thermal conduction in the solid (excluding the contributions of thermal radiation)) could be approximated by the conduction in the rods. The effective one-dimensional thermal conductivity $\lambda_{eff}$ in a direction parallel to the coordinates axis of the volume element is then determined by the conduction of only the rods parallel to this axis. Taking for example the direction of the z-axis of the volume element the heat flux through the cell boundary is the heat flux through one single rod. The other two rods are perpendicular to the direction of the energy flow and therefore do not contribute to the thermal conduction. The energy flow by thermal conduction for a single rod is

$$Q_{cond} = A_{cs,rod} \cdot \lambda_{mat} \cdot \frac{dT}{dz} \tag{46}$$

with $A_{cs,rod}$ being the cross-section area of the rod and $\lambda_{mat}$ the thermal conductivity of the material (e.g. alumina). The above energy flow could also be expressed with the effective conductivity for the cell as follows:

$$Q_{cond} = A_{cell} \cdot \lambda_{eff} \cdot \frac{dT}{dz} \tag{47}$$

with $A_{cell}$ being the area of one side of the volume element. Combining both equations results in the correlation for the effective conductivity:

$$\lambda_{eff} = \frac{A_{cs,rod}}{A_{cell}} \cdot \lambda_{mat} \tag{48}$$

With the definition of the cross-section area of a rod

$$A_{cs,rod} = \frac{\pi}{4} \cdot d^2 \tag{49}$$

and the definition of the cell area

$$A_{cell} = s^2 \tag{50}$$

this equation could be rewritten as

$$\lambda_{eff} = \frac{\pi}{4} \cdot \left(\frac{d}{s}\right)^2 \cdot \lambda_{mat} \tag{51}$$

or using the porosity

$$\lambda_{eff} = \frac{1}{3} \cdot (1 - \psi) \cdot \lambda_{mat} \tag{52}$$

For the derivation of radiative properties collimated irradiation parallel to one rod is assumed. The influence of this rod for interaction with radiation could then be neglected since the projected area in the plane perpendicular to the ray direction is small compared to the projections of the other two rods. For simplicity reasons only the attenuation of a collimated irradation is considered. Scattering or reflection effects are neglected. This assumption is justified since a good absorber is quite black, having little reflection and scattering. The reduction in radiation intensity after passing a single cell could then be described by the correlation

$$\frac{I}{I_0} = \frac{A_{pr,c} - A_{pr,r}}{A_{pr,c}} \tag{53}$$

with the projected area of the cell

$$A_{pr,c} = s^2 \tag{54}$$

and the projected area of the two rods

$$A_{pr,r} = 2 \cdot s \cdot d \tag{55}$$

With these definitions equation (53) could be rewritten as

$$\frac{I}{I_0} = 1 - 2 \cdot \frac{d}{s} \tag{56}$$

Using the definition of the extinction coefficient for the attenuation by the cubic volume element leads to the expression

$$k_t = -\frac{1}{s} \cdot \ln \frac{I}{I_0} \tag{57}$$

Using equations (36), (56) this could be rewritten as

$$k_t = -\frac{1}{s} \cdot \ln(1 - 2 \cdot \frac{d}{s}) \tag{58}$$

Two conclusions can be made from these correlations:

1. **for constant porosity material:** This is equivalent to a material with constant bulk density. From equation (40) it is evident that then the ratio d/s should be constant for various PPI-numbers. As expressed in (43) on page 5, the specific surface area per unit volume is then directly proportional to the PPI-number. On one hand, this surface area is equivalent to the convective heat transfe area. On the other hand, the catalyst loading is also expected to depend linearly on PPI-number. This holds under the assumption of constant catalyst mass per unit volume of the washcoat and of constant washcoat thickness. Under this assumption, the total catalyst loading is directly proportional to the specific surface area per unit volume. Furthermore, the extinction coefficient is also proportional to the PPI-number, as defined by equation (58).

2. **for variable porosity material:** For a foam with a given PPI-number, a variation in bulk density (or porosity) results in a variation of the ratio d/s with a proportionality of

$$\rho_{bulk} \propto (\frac{d}{s})^2 \tag{59}$$

The specific surface area per unit volume is then proportional to the square root of the bulk density. For example, an increase in porosity from 80% to 90% decreases the specific area by a factor of 0.707. As it is known (e.g. from heat transfer correlations for single wires), reducing the diameter d of the webs generally increases the convective heat transfer coefficient. This offsets partially the decrease in heat transfer area.

For the extinction coefficient, the following proportionality could be derived

$$k_t \propto -\ln(1 - 2 \cdot \sqrt{\rho_{bulk}}) \tag{60}$$

An increase in porosity from 80% (d/s = 0.291) to 90% (d/s = 0.206) results in a decrease of extinction coefficient by a factor of 0.609.

It should be stated once again that these correlations serve only as general trends due to the simplifications mentioned above. Nevertheless, they are helpful in understanding the char-

acteristics of porous absorber materials. Further research work is necessary to determine how well these correlations describe the 'real' structure.